COLD, WARM, AND HOT GAS IN THE LATE-STAGE MERGER NGC 7252

J. E. Hibbard

Astronomy Department, Columbia University, 538 West 120 Street, New York, New York 10027
Electronic mail: hibbard@parsifal.phys.columbia.edu

Puragra Guhathakurta[1]

Department of Astrophysical Sciences, Princeton University, Peyton Hall, Princeton, New Jersey 08544-1001

J. H. van Gorkom

Astronomy Department, Columbia University, 538 West 120 Street, New York, New York 10027

François Schweizer

Department of Terrestrial Magnetism, Carnegie Institution of Washington, 5241 Broad Branch Road NW, Washington, DC 20015-1305
Received 1993 July 20; revised 1993 September 23

ABSTRACT

We present the first observations of the neutral hydrogen distribution and x-ray emission in the prototypical merger remnant NGC 7252, the "Atoms-for-Peace" galaxy. These data are supplemented by accurate B and R surface photometry, reaching a limit of $\mu_B = 26.5$ mag arcsec^{-2}, and images taken through a narrow-band Hα filter. We find all of the $2 \times 10^9\ h^{-2}\ \mathcal{M}_\odot$ of atomic gas to be restricted to the outer, tidal regions of this system ($H_0 = 100\ h$ km s^{-1} Mpc^{-1}). By contrast, the molecular gas traced by the ^{12}CO($1 \rightarrow 0$) map of Wang $et\ al.$ [ApJ, 396, 510 (1992)] is confined to an inner rotating disk of radius $7''$ and has an Hα counterpart. The gap between the atomic and molecular gas distributions is filled in by diffuse Hα emission and perhaps by x-ray emission. The velocity field of the atomic gas in the tidal tails indicates that they are swinging through space in the same sense as the rotation of the inner gas disk. The H I at the apparent base of the northwestern tail seems to be falling back toward the main body of the galaxy, yet there is no H I associated with this main stellar body: This suggests ongoing efficient conversion of the atomic gas into other phases in this region. The Hα velocity anomalies previously found in the remnant body may be produced in part by the combination of tail-related, noncircular motions and the inner gas-disk rotation. Both tidal tails have bluer $B-R$ colors than the main body of the remnant, with the bluest regions coinciding with peaks in the gas column density. Each tail contains one giant H II region near the end of its optical light distribution. These H II regions are associated with large concentrations of gas and stars that approach the sizes and gas contents of dwarf galaxies. The H I extends beyond the end of the optical tails and reaches projected distances of 62 h^{-1} kpc east and 120 h^{-1} kpc northwest from the center. We discuss the possible relevance of these data to: (1) the transformation of merged spirals into ellipticals; (2) the generation of ripples by returning tidal material; and (3) the formation of bound stellar systems from tidally torn material.

1. INTRODUCTION

Over two decades ago, Toomre & Toomre (1972, hereafter referred to as TT) presented simple numerical models that demonstrated that gravitational interactions between galaxies could generate tidal features, such as the tails and bridges resplendent in Arp's (1966) Atlas, without the need to invoke either explosive or exotic electromagnetic forces. Both TT and Toomre (1977) proposed that strong collisions between disk galaxies would lead to orbital decay and eventual mergers. A sequence of 11 peculiar galaxies sketched by Toomre (1977) illustrated how the final object might feature a single relaxed body and two tidal appendages fading into the background with the passage of time: This most advanced stage of the proposed merging se-

quence was occupied by the galaxy NGC 7252 (Arp 226). The implied end-product was an elliptical galaxy.

Schweizer (1978, hereafter referred to as S78) defined five observational characteristics that unambiguously identified NGC 7252 as a late-stage merger: two roughly symmetric tails moving in opposite directions, a single relaxed nucleus, chaotic motions in the main body, the presence of faint loops and ripples in the outer parts of the main body, and its relative isolation from other likely perturbing galaxies. A more detailed photographic, spectroscopic, and photometric study of this system (Schweizer 1982, hereafter referred to as S82) revealed a number of striking new characteristics which strengthened the merger-to-elliptical hypothesis (see plate 1 of S82 for a state-of-the-art photograph of this galaxy).

One of these new characteristics is the blue portion of the optical spectrum of the main body. It shows strong

---

[1]Hubble Fellow.

Balmer absorption lines indicative of an intermediate-age population, superimposed upon Ca II H and K lines and metal bands revealing an underlying old population. This so-called "$E+A$" or "poststarburst" spectral type (Dressler & Gunn 1983) is seen out to at least 14″ and led S82 to conclude that the starburst triggered by the merger affects the whole body rather than just the central regions. Such spectra are now known to occur frequently among nearby objects suspected of being mergers on the basis of their disturbed morphology (Schweizer 1990; Kennicutt 1992).

Another unexpected characteristic is the radial light distribution of this chaotic galaxy. Despite the loops and other fine structure, concentric aperture photometry reveals that the azimuthally averaged radial brightness profile closely resembles that of an elliptical galaxy.

A third surprising discovery made by S78 was the strange line-of-sight motion of the ionized gas surrounding the central gas disk. The gas disk itself exhibits regular rotation along its major axis out to ~5″. The rotation is in the same sense as the motions of the H II regions in the tidal tails much further out (S78; S82). Recent Owens Valley Radio Observatory (OVRO) ^{12}CO($1\rightarrow0$) synthesis observations of the central 1′ of NGC 7252 (Wang *et al.* 1992, hereafter referred to as WSS) have revealed molecular gas located within a 7″ radius that shares the same sense of rotation as this ionized-gas disk. Beyond 10″ along the major axis, however, the sense of motion of the ionized gas reverses. A corresponding velocity anomaly occurs along the minor axis: No rotation is observed along the minor axis in the central ionized-gas disk itself, but large velocities occur at ~5″–20″ beyond this disk. The chaotic kinematics of the ionized gas are probably a result of the violent encounter that has fashioned this galaxy.

On deep photographs, NGC 7252's eastern and northwestern tidal tails appear to stretch ~100 h^{-1} kpc from the center, splendid vestiges of the two original disk galaxies. The essential features of this two-tailed, single-nucleus morphology have been reproduced with a simple model of two merging disk galaxies by Borne & Richstone (1991), and with a more sophisticated, fully self-consistent N-body code by Mihos *et al.* (1993). These simulations succeed in reproducing the oscillating behavior of velocities along the major axis and the nonzero velocities at larger radii along the minor axis, but require the interacting galaxies to be initially on a close, short-period orbit with an apocentric separation smaller than the diameter of a single galaxy.

Single-dish radio and millimeter-wave observations by Dupraz *et al.* (1990) have revealed significant quantities of neutral atomic hydrogen ($1.9\times10^9 \ h^{-2} \ \mathcal{M}_\odot$) and molecular gas ($3.5\times10^9 \ h^{-2} \ \alpha_{CO}\mathcal{M}_\odot$)[2] in NGC 7252 ($H_0=100 \ h$ km s^{-1} Mpc^{-1}). These masses are large compared to the typical gas contents of E and S0 galaxies (Knapp *et al.*

1985; Lees *et al.* 1991). The implication is that, if NGC 7252 is to resemble an elliptical-like system after the tidal tails and loops disperse, it must somehow rid itself of the majority of this gas.

We have undertaken an investigation of the distribution and kinematics of the H I in NGC 7252 to help understand the encounter dynamics and to explore how this merger might go about ridding itself of its ample supply of cold gas. The present data are part of a broader study of the fate of gas in galaxies at progressive stages of merging, with particular emphasis on the gas distribution in the outer tidal regions (Hibbard & van Gorkom 1994). We combine results from several different wavelength regimes to address this question. Radio synthesis observations have been used to obtain good spatial resolution, high sensitivity to extended gas emission, and line-of-sight velocity information. Broad- and narrow-band optical images are used to delineate the underlying stellar distribution and to identify regions of recent star formation. X-ray observations have been obtained to investigate the hot gas content of the remnant.

Mergers are important laboratories for studying a broad range of astrophysical phenomena, from the formation to the transformation of galaxies. Neutral hydrogen studies like the one presented here are particularly suited for gaining insight into these questions by providing complete velocity mapping of the tidal features. These can be used to constrain the increasingly sophisticated numerical simulations in progress and to help elucidate the past and future evolution of such systems.

This paper is structured as follows: Section 2 describes our observations of NGC 7252; Sec. 3 contains a study of the various gas components and of the kinematics of the H I, separately for the inner and outer regions; Sec. 4 discusses these data and compares them to previous observational and theoretical work, with the goal of understanding the fate of the gas in this merger; and Sec. 5 summarizes the main results and implications.

2. OBSERVATIONS AND DATA REDUCTION

The new data for NGC 7252 consist of H I spectral-line observations using the Very Large Array[3] (VLA), *ROSAT* Position Sensitive Proportional Counter (PSPC) x-ray observations, optical broadband photometry done at the Cerro Tololo Inter-American Observatory[4] (CTIO), and narrow-band Hα images obtained at the Kitt Peak National Observatory[4] (KPNO). Tables 1–3 list the relevant instrumental and observational parameters. Since the data acquisition and reduction techniques are explained in detail by Hibbard & van Gorkom (1994), we limit ourselves here to a brief summary.

---

[2]Molecular hydrogen column densities N_{H_2} and masses are calculated from the integrated ^{12}CO($1\rightarrow0$) emissivity $\int T_b dv$ (where T_b is the brightness temperature in K and the integral is over the line, with the velocity v expressed in km s^{-1}) using a conversion factor α_{CO} such that $N_{H_2}=4\times10^{20}\alpha_{CO}\int T_b dv$ cm^{-2}. Best estimates of α_{CO} range from 0.5 to 1.5 under most conditions (Maloney 1989).

TABLE 1. VLA observing parameters.

Phase Center (α_{1950} δ_{1950})	$22^h17^m57.9^s$	$-24°55'50''$	
Velocity Center (Heliocentric)		4749 km s^{-1}	
Primary Beam (FWHM)		30'	
Phase Calibrator		2208–188	
Flux Calibrator		3C48	

Array	D	CnB[a]	C+D[b]
Date	Dec 89	Oct 90	—
Synthesized Beam			
— FWHM: Major Axis × Minor Axis	$96''\times52''$	$15''\times15''$	$27''\times16''$
— Position Angle (East of North)	$-1°2$	$+0°$	$-18°6$
Bandwidth (MHz)	6.25	3.25	2.9
Number of Channels	32	63	15
Channel Separation (km s^{-1})	42.5	10.6	42.5
Time on Source (hrs)	6.8	22.4	29.2
Noise Level (1σ)			
— Flux Density (mJy beam^{-1})	0.37	0.33	0.20
— Column Density (10^{19} cm^{-2} beam^{-1} ch^{-1})	0.3	1.7	2.2
1 K Equivalent (mJy beam^{-1})	0.12	2.7	1.4

Notes to TABLE 1.

[a] The hybrid CnB-array has a long north arm, which is particularly useful for southern

sources such as NGC 7252. For the sake of brevity in the text, we refer to this set of

observations as the C-array data.

[b] The combined CnB- and D-array data set is referred to as the C+D data.

2.1 Radio Observations

The H I observations were carried out with the VLA in its spectral-line mode. The galaxy was observed in two configurations: the 1.3 km D-array configuration and the 3 km C-array configuration with the antennas of the north arm in the 10 km B-array configuration to improve the north–south angular resolution, thus compensating for the low declination of NGC 7252. (The latter configuration is commonly known as the CnB array, but we shall refer to it as the C array for the sake of simplicity). The D-array observations consisted of two runs of 4 h each, and the C-array observations consisted of seven 4 h runs.

TABLE 2. CTIO/KPNO observing parameters.

Date	Sep 90	Aug 91
Telescope	CTIO 4m	KPNO 2.1m
Detector	TI 800	ST1k
Readout Mode	binned 2×2	binned 2×2
Focal Ratio	f/2.7	f/7.5
Field of View:		
— Single CCD frame	4.0×4.0	4.6×4.6
— Final Image	$12'\times8'$	$12'\times8'$
Pixel Size	0.600	0.533
Filters	B_J, R_t	R, Hα6649
λ_0	4500 Å, 6500 Å	6500 Å, 6649 Å
$\Delta\lambda$	1500 Å, 1400 Å	1280 Å, 70 Å
Seeing	1.2	2.0
Sky Brightness (B, R) (mag arcsec^{-2})	22.0, 20.5	—
1σ Sky Noise (B, R) (mag arcsec^{-2})	27.7, 26.9	—
Effective Exposure Time	$\sim4\times100$ s	300 s, 3×1200 s

The D-array observations were exploratory and used a 6.25 MHz bandwidth, corresponding to a total velocity range of 1300 km s^{-1}. On-line Hanning smoothing has been applied to the data after which every other channel is

TABLE 3. *ROSAT* observing parameters/spectral fit.

Date	Nov–Dec 92
Detector	PSPC 2 (B)
Field of View	$62'\times62'$
Energy Range	0.1–2.4 keV
Time on Source	17,381 s
Source Counts	164±22
Background Flux Density	1.2×10^{-3} counts s^{-1} arcmin^{-2}
Background Noise (1σ)	5.8×10^{-4} counts s^{-1} arcmin^{-2}

Model[a]	$\log(N_{HI})$[b] (cm^{-2})	kT (keV)	$L_{X,[0.1-2.4\,keV]}$ ($10^{40} h^{-2}$ erg s^{-1})
Thermal Bremsstrahlung	20.3	5.0	2.0±0.1
Raymond-Smith Plasma	20.3	1.0	1.7±0.1

Notes to TABLE 3

[a]Models used to calculate x-ray luminosity chosen from the study of Fabbiano *et al.* (1992). The thermal bremsstrahlung model with an emission temperature of 5 keV is used to compare NGC 7252 with the x-ray luminosities of spiral galaxies, while a Raymond–Smith (1977) optically thin plasma model with solar metal abundance and an emission temperature of 1 keV is used to compare it with ellipticals.

[b]The Galactic absorbing column density N_{HI} is held fixed at the value given in Stark (1992).

discarded, leaving a set of 31 independent channels centered at 4749 km s^{-1} and spaced by 42.5 km s^{-1}. (All radial velocities quoted in this paper are heliocentric). The C-array observations used 63 channels and a 3.25 MHz bandwidth to achieve 10.6 km s^{-1} velocity resolution. The C-array data have been Hanning smoothed to 42.5 km s^{-1} resolution and combined with the D-array data in the UV plane to yield a C+D dataset. It is this combined dataset that will be used primarily throughout the present paper due to its superior sensitivity, though the C-array data alone will occasionally be used to take advantage of its higher velocity resolution. The H I flux scale was set using 3C48 as the primary calibrator, adopting a flux of 16.25 Jy at 1.398 GHz (Baars *et al.* 1977).

2.2 Optical Observations

The broadband optical data consist of B_J and R_t images obtained with a CCD camera on the CTIO 4 m telescope (see Tyson & Seitzer 1988 for a description of this filter system). The CTIO data were obtained under photometric conditions using a step-and-stare technique, in which the telescope is moved by about 1′ between subsequent exposures (each has a 4′×4′ field of view). A total of 19 individual 100 s exposures, in each of B_J and R_t, were needed in order to cover a 12′×8′ region. Generous overlap between the different exposures ensures that each portion of the galaxy is imaged about four times on average—an effective exposure time of ~400 s. Extreme care is taken to flatfield the exposures, using dome flats and dark sky flats, and to monitor and correct for temporal variations in the night sky brightness. A mosaic image is then constructed from all the images in a given filter using an extension of the technique developed by Guhathakurta & Tyson (1989). The magnitude zero points are determined with the help of exposures on fields containing photometric standards. The B_J and R_t magnitudes are converted to Johnson/Cousins B and R magnitudes via the transformation equations given by Gould *et al.* (1992). The probable errors in the zero points of the B, R, and $B-R$ scales are 0.05, 0.03, and 0.06 mag, respectively. The accuracy of the flatfielding and the high degree of matching of the individual frame edges in the final mosaic image assure us that the background varies by less than 0.1% across the mosaic—systematic color errors due to background variations are ≲0.05 mag over the region of interest.

Colors are computed for all regions of the galaxy with surface brightnesses greater than three times the sky noise (as measured on the original, unsmoothed image), corresponding to $\mu_R < 25.7$ mag arcsec^{-2} and $\mu_B < 26.5$ mag arcsec^{-2}. In order to do this, stars are removed from both the B_J and R_t images using standard techniques of DAOPHOT (Stetson 1987) and poorly subtracted pixels are blanked. A $B-R$ color map is then formed by median smoothing the image with a 5″×5″ filter while ignoring masked pixels. The errors in color due to photon statistics

alone are 0.03 mag for the brighter features and ≲0.05 mag for all regions of interest.

Three Hα images, of 1200 s exposure each, have been obtained using the 2.1 m telescope at KPNO: One each of the H II regions in either tidal tail and one of the main body. A narrow-band Hα filter centered at λ6649 Å, 16 Å off the redshifted Hα line center, has been used. The filter passband is 70 Å wide and thus includes emission from the [N II] $\lambda\lambda$ 6548 Å, 6584 Å lines (rest wavelengths). In order to subtract the continuum, broadband R exposures of 300 s each were obtained immediately before or after the Hα frames. The Hα data were obtained under nonphotometric sky conditions, and remain uncalibrated.

Finally, the radio and optical images have been transformed to a common coordinate system. Absolute astrometry of the optical images has been done via the positions of four stars in the Hubble Space Telescope Guide Star Catalog. The error in relative astrometry between the optical and radio data is likely to be ≲1″ (see Sec. 3.1.1) and the different optical images are aligned with one another to ≲0.″3.

2.3 X-ray Observations

The *ROSAT* PSPC observations were obtained in 1992 December and 1993 January and amount to 17 381 s of data centered on NGC 7252. This image has been calibrated using standard procedures in the PROS environment of NOAO's Image Reduction and Analysis Facility. In this paper, we only discuss the broadband image corresponding to an energy range of 0.1–2.4 keV.

The x-ray counts from NGC 7252 are measured within a circular aperture of radius 120″ after subtracting the background from a similar area off the source. Due to the low number of counts in the individual energy bins, we do not fit the spectral energy distribution. Instead, we adopt specific models for the emission mechanisms for the purposes of computing the x-ray luminosity: (1) a thermal bremsstrahlung model with an emission temperature $kT=5$ keV; and (2) a Raymond–Smith (1977) model with $kT=1$ keV and solar metal abundance. These models (and the specific model parameters adopted) have been chosen to be the same as those used to analyze EINSTEIN x-ray data on a large sample of spirals and ellipticals, respectively (Fabbiano *et al.* 1992), in order that the x-ray luminosity of NGC 7252 may be compared directly with this dataset. The thermal bremsstrahlung spectrum is typical of discrete galactic sources, such as x-ray binaries and supernova remnants, while the Raymond–Smith model characterizes emission from a hot, optically thin plasma. We do not consider a power-law model as there is no evidence for an active nucleus in the center of NGC 7252 in either its optical spectrum or its far-infrared luminosity.

Luminosities are obtained by integrating the above models over the desired energy band, after correcting for absorption by a column density of Galactic atomic hydrogen $N_{\rm H\,I}$. We adopt the value of $N_{\rm H\,I}$ measured by Stark

TABLE 4. Global properties of NGC 7252.

(1) Region	(2) M_{HI} ($10^8\,h^{-2}\,M_\odot$)	(3) Velocity Range (km s^{-1})	(4) Projected Distance (h^{-1} kpc)	(5) L_B ($10^8\,h^{-2}\,L_\odot$)	(6) M_{HI}/L_B ($M_\odot/L_\odot$)
NW tail	11.7±0.3	4674–4877	120	15.1	0.77
E tail	6.2±0.2	4743–4835	62	4.8	1.29
W loop	2.2±0.1	4521–4632	12	6.2	0.35
Companion^a	7.6±0.3	4759–4824	170	—	—

Total N7252:

M_{HI}	$2.0\times10^9\,h^{-2}\,M_\odot$
$M_{\mathrm{H_2}}{}^b$	$3.5\times10^9\,h^{-2}\,\alpha_{\mathrm{CO}}\,M_\odot$
L_B	$2.9\times10^{10}\,h^{-2}\,L_\odot$
B	12.71 mag
$L_{\mathrm{X},[0.2-4.0\,\mathrm{keV}]}$ (TB)^c	$2.4\pm0.1\times10^{40}\,h^{-2}$ erg s^{-1}
$L_{\mathrm{X},[0.2-4.0\,\mathrm{keV}]}$ (RS)^c	$1.5\pm0.1\times10^{40}\,h^{-2}$ erg s^{-1}
$L_{\mathrm{FIR}}{}^d$	$2.3\times10^{10}\,h^{-2}\,L_\odot$
M_{HI}/L_B	$0.07\,M_\odot/L_\odot$
$M_{\mathrm{H_2}}/L_B$	$0.12\,\alpha_{\mathrm{CO}}\,M_\odot/L_\odot$
L_{FIR}/L_B	0.9
$L_{\mathrm{FIR}}/M_{\mathrm{H_2}}$	$6.6\,\alpha_{\mathrm{CO}}{}^{-1}\,L_\odot/M_\odot$

Notes to TABLE 4.

(1) Region name.

(2) Integrated H I mass, calculated using: $M_{\mathrm{HI}} = 2.35\times10^5\,D_{\mathrm{Mpc}}^2\int S_{\mathrm{HI}}dv\ M_\odot$, where D_{Mpc} is the distance in Mpc, and $\int S_{\mathrm{HI}}dv$ is the integrated H I emissivity, in Jy km s^{-1}. We adopt $47.4\,h^{-1}$ Mpc as the distance to NGC 7252.

(3) Range of H I velocities (heliocentric), taken from the first-moment image. The uncertainty is ±3 km s^{-1}.

(4) Maximum projected distance of the H I from the center of NGC 7252.

(5) Total blue luminosity.

(6) Ratio of mass of atomic hydrogen to blue luminosity.

^{a} Low surface brightness barred spiral companion located at $\alpha_{1950} = 22^h18^m33\overset{s}{.}2$, $\delta_{1950} = -24°46'35''$ and $v_{\mathrm{hel}} = 4794$ km s^{-1}. Its luminosity is not listed since the optical data were obtained under non-photometric conditions.

^{b} Molecular hydrogen mass from Dupraz *et al.* (1990). The integrated ^{12}CO$(1\to0)$ emissivity $\int T_b dv$ (in K km s^{-1}) is converted to an equivalent molecular hydrogen column density: $N_{\mathrm{H_2}} = 4\times10^{20}\,\alpha_{\mathrm{CO}}\int T_b dv$ cm^{-2}. Best estimates of the conversion factor α_{CO} range from 0.5 to 1.5 under most conditions (Maloney 1989).

^{c} Estimated X-ray luminosity of NGC 7252 in the 0.2–4.0 keV range of the *EINSTEIN* observatory based on the models given in Table 3: TB = Thermal Bremsstrahlung; RS = Raymond-Smith (1977). The TB and RS values may be compared directly to the mean values of $5.8\times10^{39}\,h^{-2}$ erg s^{-1} and $6.5\times10^{40}\,h^{-2}$ erg s^{-1} for spirals and ellipticals, respectively, of the same blue luminosity (Fabbiano *et al.* 1992).

^{d} Far infrared luminosity from Dupraz *et al.* (1990).

(1992), but note that this measurement was made with a 2° beam size; the actual value of $N_{\mathrm{H\,I}}$ at the center of NGC 7252 may thus be quite different from that used here. The *ROSAT* observational parameters and the results of the x-ray luminosity calculations are listed in Table 3. The x-ray luminosity of NGC 7252 in the 0.2–4.0 keV band $L_{\mathrm{x},[0.2-4.0\,\mathrm{keV}]}$, appropriate for comparisons with existing EINSTEIN measurements, is given in Table 4. Changing $N_{\mathrm{H\,I}}$ by a factor of 10 or kT by a factor of 2 for either model results in a value of $L_{\mathrm{x},[0.2-4.0\,\mathrm{keV}]}$ that is within $\pm20\%$ of the mean value listed in Table 4. To the extent that the x-ray emission from galaxies is characterized by

these models, this should be a good estimate of the allowable range in the x-ray luminosity.

3. RESULTS

3.1 Global H I Properties

3.1.1 Spatial distribution

Figure 1 (Plate 20) presents the neutral hydrogen distribution (blue), a summed optical $B+R$ mosaic image showing the starlight (green), and a continuum-subtracted Hα image of NGC 7252 (red). The differences between the distributions of the two gas phases, and between the distributions of the gas and stars, are striking. In particular, note that the H I is confined almost entirely to the outer, tidal regions. We shall show shortly that the atomic gas which appears near the nucleus (in projection) is likely to belong to features outside the main body, as evidence by its kinematics. The ionized gas is concentrated in four different locations: at the center, in the two bright H II regions in the tidal tails, and in the western loop. (Additional red pixels are due to stars that were saturated on the R CCD frame).

We identify three main components of H I: The northwestern (NW) tail which appears to cross in front of the remnant and has a projected length of 520″ ($120\,h^{-1}$ kpc); the eastern (E) tail which reaches a projected distance of 270″ ($62\,h^{-1}$ kpc); and the western (W) loop, a bright filament with several optical knots that reaches a maximum projected distance of 50″ ($12\,h^{-1}$ kpc) directly west of the center. The VLA observations yield a 21 cm line flux of 4.0 Jy km s^{-1} for the entire galaxy, corresponding to a total H I mass of $2.0\times10^{9}\,h^{-2}\,\mathcal{M}_{\odot}$. This flux agrees with the single-dish measurement of Dupraz *et al.* (1990) within observational errors. Table 4 summarizes some of the global properties of NGC 7252. We adopt $D=47.4\,h^{-1}$ Mpc as the distance to NGC 7252.

There is a 21 cm continuum source coincident with the center of NGC 7252. The excellent agreement between the positions of this radio source, the central Hα disk and of the optical center of the galaxy indicates that the relative astrometry between the radio and optical datasets is better than 1″. The central radio source has a flux of 19 mJy at 1.398 GHz and is possibly slightly resolved in the C-array image. There is no evidence for absorption against this source, placing an upper limit (3σ, per channel) on the column density of absorbing gas in front of the central continuum source: $N_{\mathrm{H\,I}}\lesssim10^{18}T_s\,\mathrm{cm}^{-2}$, where T_s is the spin temperature of the H I. A more interesting limit of the column density of atomic gas can be obtained from the lack of H I emission within the body of the remnant away from the continuum source. Throughout the remnant body, the column density of H I is less than $5\times10^{19}\,\mathrm{cm}^{-2}$. A comparison of this upper limit with the H I detected in the W loop and innermost regions of the NW tail shows that the surface density of the H I drops by at least a factor of 4 between these outer regions and the central body.

The VLA observations also reveal an uncatalogued companion galaxy about $12'\approx170\,h^{-1}$ kpc to the northeast of NGC 7252, centered at 4794 km s^{-1}. An 80 min
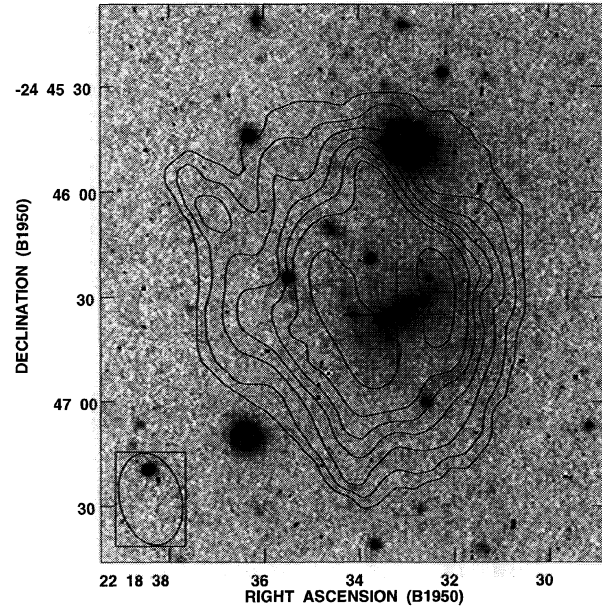

FIG. 2. A KPNO 2.1 m R-band image of the companion to NGC 7252 in negative greyscale with overlaid H I gas column density contours from the VLA C+D data indicating levels of (5, 10, 15, 20, 25, 30, 40)×10^{19} cm^{-2}. The H I beamwidth (FWHM): 26″×16″ is shown in the lower left. This companion, a low surface brightness barred spiral, is located 12′ to the northwest of NGC 7252 (projected distance of 170 h^{-1} kpc) and is separated from it in velocity by 54 km s^{-1}. The geometry of the tidal tails in NGC 7252 and the estimated low mass of this companion make it highly improbably that it is responsible for the damage seen in NGC 7252.

KPNO 2.1 m optical R-band image shows this companion to be a low surface brightness barred spiral. Figure 2 presents a (negative) greyscale reproduction of the R image with H I column density contours overlaid. Based on a 21 cm linewidth of 128 km s^{-1} (measured at 20% of peak flux) and a disk inclination of ~30°–50°, we derive a dynamical mass of $1-3\times10^{10}\,h^{-1}\,\mathcal{M}_{\odot}$ within a radius of 7 h^{-1} kpc. Although the effect of this companion on the encounter is difficult to judge in the absence of detailed orbital information, we do know that *no* outside perturber could have raised the two tidal tails of NGC 7252. Had an external perturber been responsible, the tails would have been separated by 180° and approximately symmetric and coplanar. Both the apparent angle between the tails of NGC 7252 and the asymmetric tail velocities show that this is not the case.

3.1.2 Kinematics

Figure 3 shows the individual channel maps of the C+D dataset in an $11'\times14'$ region centered on NGC 7252 with a channel spacing of 42.5 km s^{-1}. These maps show that the velocities vary smoothly along the tidal tails, and that the two tails and W loop form three distinct features that are localized in velocity space. There is a concentration of atomic gas in each tidal tail associated with the H II region (marked by the two extreme crosses in Fig. 3). The H I concentrations in the E tail occur to the east of
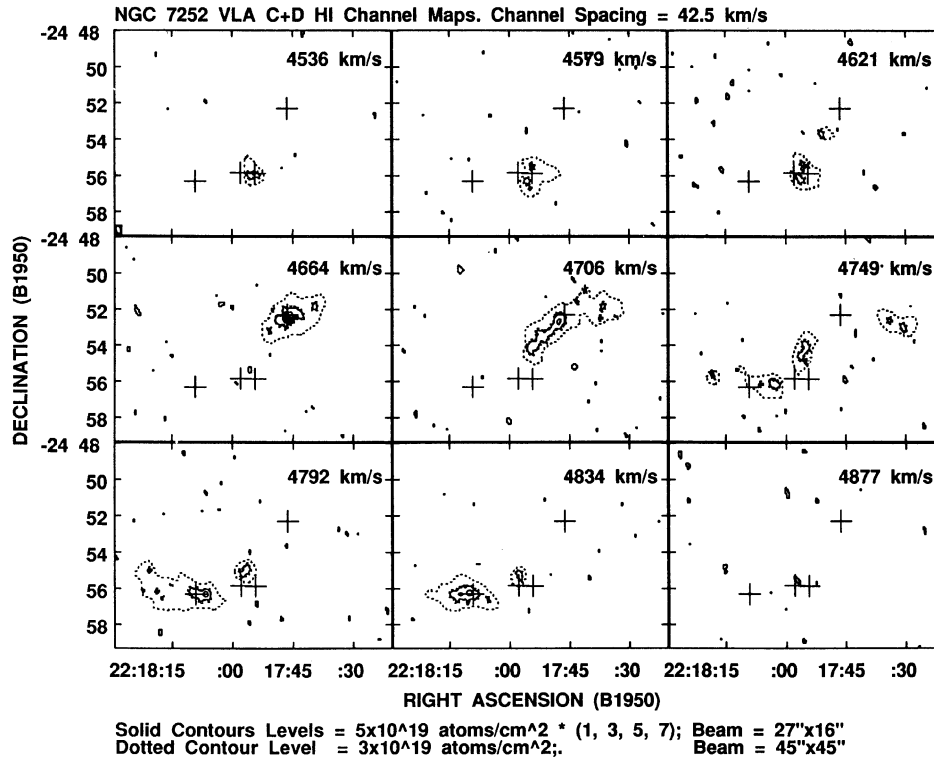
NGC 7252 VLA C+D HI Channel Maps. Channel Spacing = 42.5 km/s

FIG. 3. The H I line emission channel maps from the VLA C+D data running from 4536 km s^{-1} (bottom left panel) to 4877 km s^{-1} (top right panel). The two extreme crosses in each panel mark the locations of the H II regions in the NW and E tidal tails while those near the middle mark the remnant center (left) and the brightest H II region in the W loop (right). The solid contours are from the full resolution C+D data cube (FWHM:26″×16″) and show column densities of (5, 15, 25, 35)×10^{19} cm^{-2}. The dotted contours from the smoothed C+D data (FWHM: 45″×45″) indicate a column density of 3×10^{19} cm^{-2}. The top three panels show emission from the W loop, with a large negative velocity relative to systemic (4740 km s^{-1}); the middle panels show predominantly the (blueshifted) NW tail; and the bottom panels show redshifted H I in the E tail and at the base of the NW tail.

the H II region in the channel at 4834 km s^{-1}, and to the west of it at 4792 km s^{-1}. The concentration in the NW tail consists primarily of a single clump of 10^8 h^{-2} $\mathcal{M}_\odot$ of H I in the channel at 4664 km s^{-1}. The H II regions are examined in more detail in Sec. *3.3.2.*

Figure 4(a) presents the intensity-weighted mean H I velocity field of the entire galaxy, superimposed upon a negative greyscale image of the H I column density distribution. The three main components of H I are labeled: the two tidal tails and the W loop complex. A special note is made of the gas at the apparent base of the NW tail which is redshifted with respect to the symmetric velocity of 4740 km s^{-1} (WSS). Note that the peaks in the column density of atomic gas occur near the H II regions [two extreme crosses in Fig. 4(a)].

A position-velocity diagram for this system is shown in Fig. 4(b), directly below Fig. 4(a) and on the same spatial scale as it. This map has been constructed by summing the gas emission along the declination axis, and plotting the integrated intensity at each velocity (ordinate) as a function of the east–west component of the angular distance from the remnant center (abscissa). This mapping provides a clear picture of the smoothness and completeness of the velocity field, although it does exaggerate the velocity gradient along the NW tail and W loop due to the fact that these features do not run exactly east–west. Figure 4(b)

shows that *all of the detected H I is associated with one of the three main kinematic features.*

Figures 4(a) and 4(b) illustrate the smooth continuity of the H I velocities along the tails from the inner to the outermost regions. The E tail is redshifted relative to systematic, while most of the NW tail is blueshifted. The absolute value of the relative velocity rises as one traces the H I outwards from the center along each tidal, reaches a maximum, and then falls back again. Such smooth runs of velocity in tidal tails are reproduced in numerical simulations of mergers, which show the tails to be extended ribbons of material swinging through space (TT; also Fig. 11 of Barnes 1992). In light of these models, the observed kinematics of NGC 7252 suggest that the NW tail is swinging toward us and that the inner part of the tail crosses in front of the remnant body (a view that is supported by the presence of an obscuring dust lane and by the optical morphology presented in Sec. *3.2.1*), while the E tail crosses behind the galaxy and is swinging away from us. Thus the motions are such that the angular momentum vector everywhere along the tails points roughly toward the south.

Near the apparent base of the NW tail, the velocities are higher than systemic by up to 130 km s^{-1} (i.e., redshifted relative to center), whereas the rest of this tail has velocities lower than systemic. The occurrence of both redshifted and blueshifted velocities *on the same side of the nucleus*
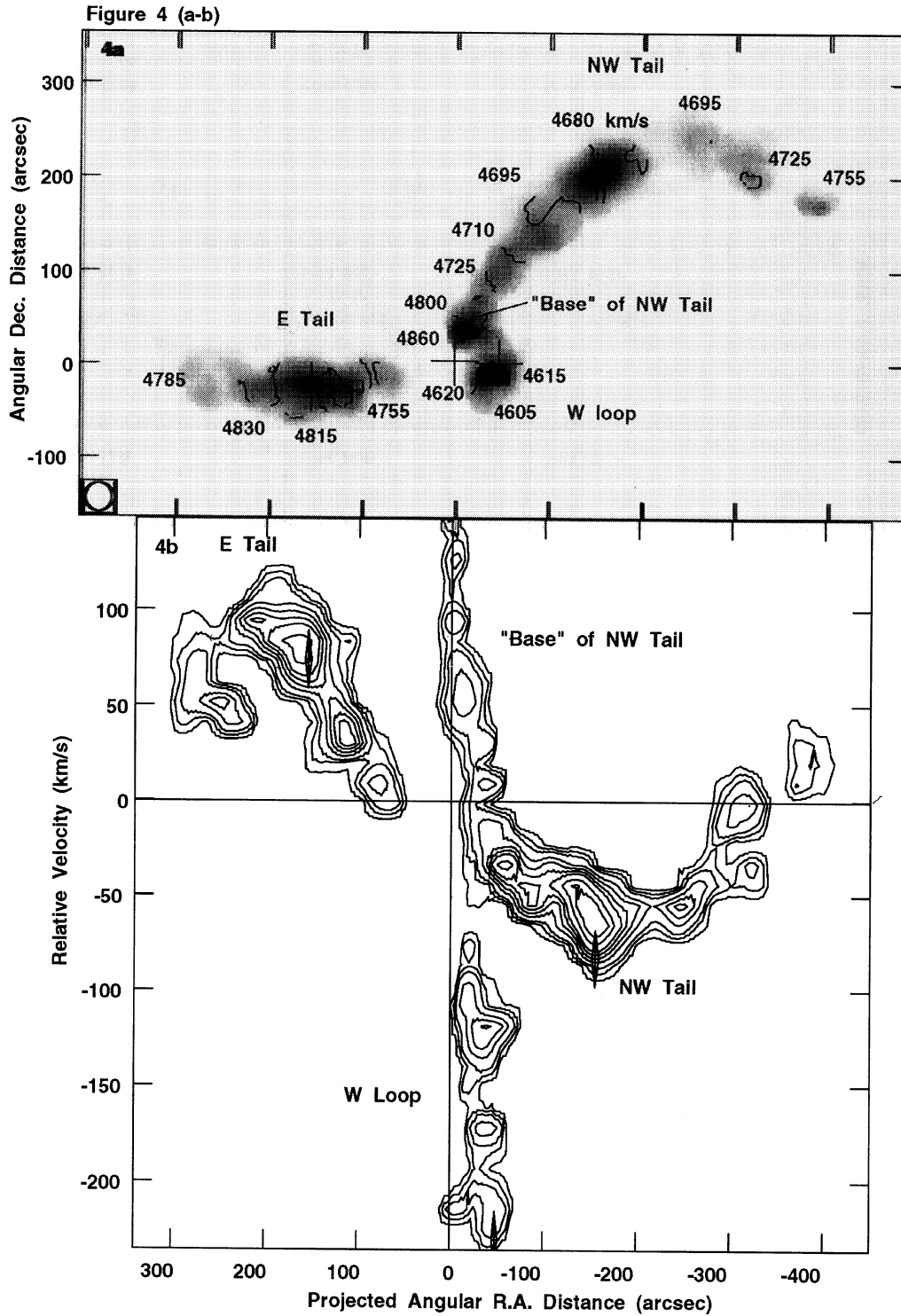
Figure 4 (a-b)

FIG. 4. The H I kinematics of NGC 7252, derived by smoothing the C-array data to a resolution of 30″. Both panels are on the same angular scale and the major kinematic features are labeled. (a) The isovelocity contours overlaid on a negative greyscale representation of the atomic gas column densities in the range 3–30×10^{19} cm^{-2}. The crosses and orientation are as in Fig. 3, and the FWHM of the beam is indicated in the lower left. (b) Position-velocity profile, obtained by integrating the H I along the declination axis. The projection of the angular distance from the center along the right ascension is plotted on the x axis and the velocity relative to systemic (4740 km s^{-1}) is plotted along the y axis. This profile tends to exaggerate the velocity gradient along the NW tail and W loop, since these features do not run east–west. The lines through the origin mark the spatial and kinematic center of the remnant as defined by the ^{12}CO(1→0) measurements of WSS. Diamonds mark the Hα measurements of the H II regions in either tail and of the W loop made by S82, with the width and height indicating the uncertainties in position and velocity, respectively. These plots illustrate the continuity of the H I features in space and velocity and show that all the detected atomic gas is associated with one of three main structures: the two tidal tails and the W loop complex. Note that the NW tail goes from being blueshifted in its outer parts to having redshifted velocities at its apparent base.

leads us to conclude that the gas near the apparent base of this tidal tail is falling back toward the remnant body (see Sec. *4.2*).

It is clear from Fig. 4(b) that the gas in the W loop is kinematically separate from the gas at the apparent base of the NW tail. Further, the combination of the E tail and the W loop forms a pattern in the position-velocity diagram that is strikingly similar to that formed by the NW tail (but turned 180° around). This suggests a possible association between the W loop and E tail. Although the H I shows no traceable connection between the two sides, the optical morphology suggests that the W loop is a natural continuation of the portion of the E tail that disappears behind the main remnant body (S82). This suggests that material in the W loop may have come from the same progenitor disk that formed the E tail.

The locations of the Hα velocity measurement made by S82 of the giant H II regions in either tail and of the brightest knot in the W loop are indicated by diamonds in Fig. 4(b). The vertical length of the diamonds corresponds to the estimated error in velocity (Schweizer 1993), while their horizontal width indicates the positional uncertainty. The H I and Hα mean velocities at the location of the E H II regions are in good agreement, but the peak in the H I column density is offset somewhat to the west of the H II region. The velocity difference at the W loop is 15 km s^{-1}, with the Hα having the more blueshifted velocity. In the NW giant H II region, the peak in the H I column density coincides with the position of the Hα emission, but the difference in velocities is 23 km s^{-1}, with the Hα again having a higher blue shift relative to systemic than the H I. Given the estimated Hα velocity errors of 10–15 km s^{-1}, the last two velocity differences may be marginally significant, but the vastly different spatial resolutions in Hα and H I complicate the comparison.

3.2 Gas in the Main Body

This section examines the distribution and kinematics of the various gas phases in the main body of the merger remnant. In particular, we search for possible clues that might explain the apparent dearth of H I in this region.

3.2.1 Spatial distribution

Figure 5 shows the main body of NGC 7252 and all the gas phase detected in it. The first three panels show various representations of the optical light with the contours of progressively cooler gas phases superimposed. The final three panels illustrate the interrelationship between these different gas phases.

In Fig. 5(a), the *ROSAT* PSPC x-ray emission in the 0.1–2.4 keV energy range is shown as contours overlaid on a positive greyscale representation of the CTIO 4 m *B*-band optical image. The peak central flux density is 6.8×10^{-3} counts s^{-1} arcmin^{-2} and corresponds to 12 times the background rms noise. The heavy contour is drawn at half the peak surface brightness. The size of the central cross indicates the resolution of the PSPC at 0.5 keV (FWHM=34″). The observed FWHM of the x-ray

emission in NGC 7252 is 39″×30″ and may thus be marginally resolved, but the situation is complicated by the fact that the PSPC spatial resolution is a function of energy.

Figure 5(b) shows the Hα emission from ionized gas in the form of contours against a white background, superimposed upon a negative greyscale image of the blue light distribution. The ionized gas is strongly concentrated toward the center, with a roughly symmetric morphology. In the outer parts of the remnant body, much of the ionized gas appears to be associated with the tidal features: An extension is seen toward the region where the NW tail crosses the face of the remnant, and a string of Hα knots lines the southern leg of the W loop to the west and southwest of the center.

About 90% of the Hα line emission is within the boundaries of the molecular-gas disk ($r < 7″$) while the rest is distributed more widely. Only about 3% of the Hα flux comes from the W loop and from the H II regions in the tails. The quoted 90% for the central component is a lower limit to the relative amount of Hα flux (and therefore of star formation) associated with the central molecular-gas disk, since extinction by dust is likely to be most severe near the center. Thus, at present, most of the star formation in NGC 7252 seems to be taking place within this central gas disk.

The distributions of optical starlight and of atomic hydrogen in and around the main body of NGC 7252 are compared in Fig. 5(c). The negative greyscale shows a model-subtracted *B* image, where the model consists of azimuthally averaged elliptical fits to the isophotes of the light distribution. Areas around stars and the brighter optical tidal features (loops, shells, and tails) have been excluded from the fit. The atomic hydrogen column density contours are superimposed on this optical image in Fig. 5(c). In contrast to the warmer gas phases, the atomic gas is confined to some of the loops in the outskirts of the main body and to the tidal tails. Further, the H I contours are offset somewhat from the peaks in the optical light, both at the apparent base of the NW tail and in the W loop.

The model-subtracted *B* image shows a considerable amount of detail that is useful for understanding the orientation of the tidal features and loops. Note that the NW tail appears to cross the face of the main body of the galaxy and perhaps connect up with the south–southeastern loop, from points A to B in Fig. 5(c). This continuity can be seen better in a sum of three high signal-to-noise masked photographic images obtained by Schweizer & Ford [1985, Fig. 2(b)]. Figure 5(c) also shows several shells some of which feature distinct radial "spokes."

Figure 5(d) presents a greyscale rendition of the spatial distribution of optical $B - R$ color in the central part of NGC 7252 with blue colors denoted by light tones and red colors by dark tones. The H I contours are again superimposed. Note that the central few pixels and a star to the north–northeast of the nucleus appear white in this figure due to the fact that they are saturated on the *R*-band CCD frame. The color map is noisy near the edges of the remnant where the *B* and *R* surface brightness goes to zero and
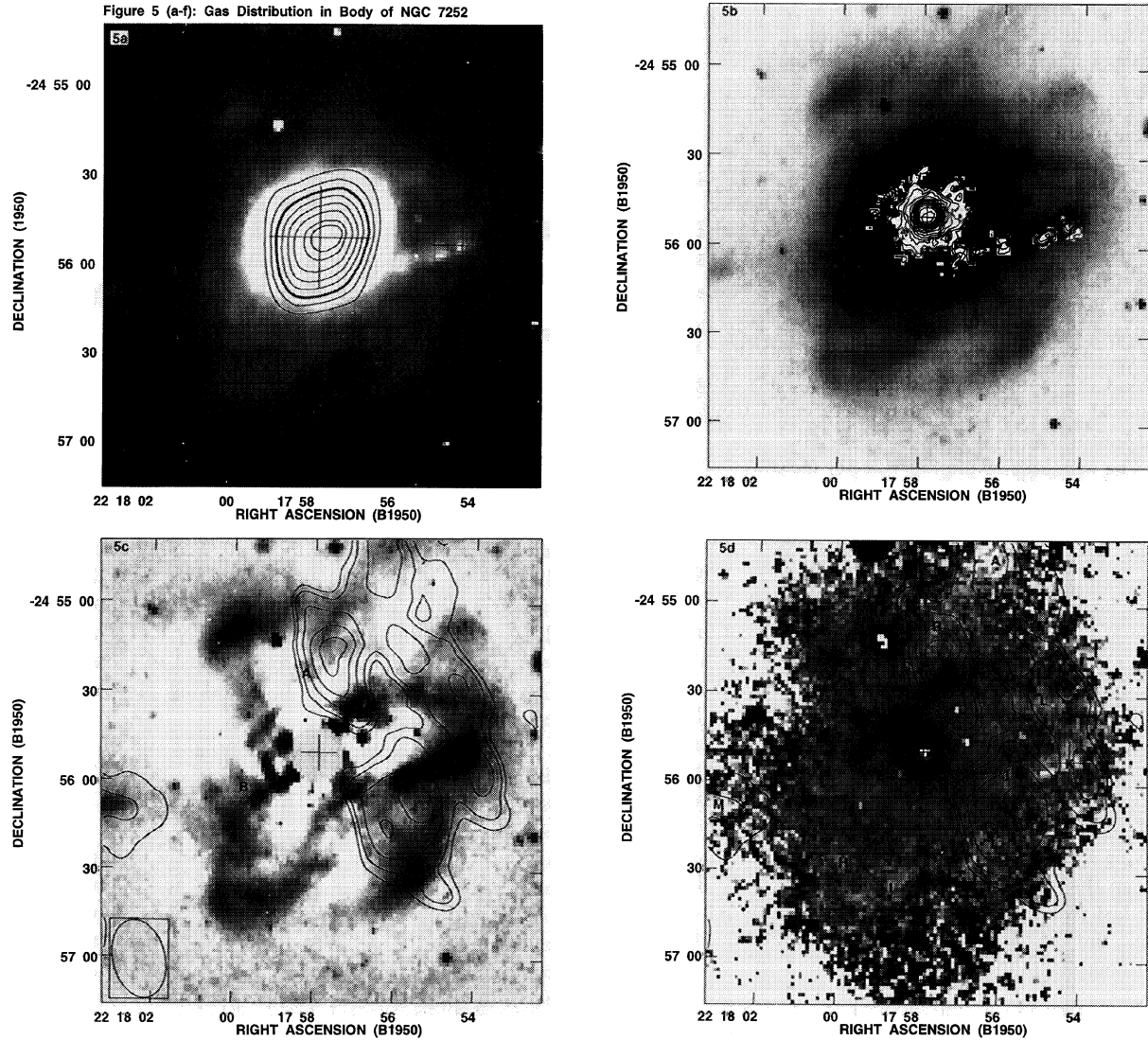
FIG. 5. Details of the gas distribution in the remnant body of NGC 7252. The crosses in each panel mark the remnant center (left) and the brightest H II region in the W loop (right). (a) Contours of the *ROSAT* PSPC x-ray emission in the 0.1–2.4 keV energy range superimposed on a positive greyscale map of the *B*-band light distribution. The contours are drawn at (0.3, 0.4, 0.5, 0.6, 0.7, 0.8, 0.9, 0.95) times the peak central flux density of 6.8×10^{-3} counts s^{-1} arcmin^{-2}. The rms background noise is 5.8×10^{-4} counts s^{-1} arcmin^{-2}. The bold contour is at half the peak brightness level. The size of the central cross indicates the nominal resolution of the PSPC (FWHM: $34'' \times 34''$ at 0.5 keV)—the hot gas may be marginally resolved by the present observations. (b) A composite of the Hα image (contours against a white background) and the *B* image (negative greyscale). The warm ionized gas is strongly concentrated toward the center, but also has a diffuse component and some Hα is seen in the W loop and near the base of the NW tail. (c) A negative greyscale image of the residual light that remains after a smooth elliptical model has been fit and subtracted from the *B*-band image (see Sec. 3.2.1). Contours of the H I column density (VLA C+D) are drawn at (7.5, 10, 15, 20, 25) $\times 10^{19}$ cm^{-2} and the beam size and shape are indicated by the ellipse in the lower left. The atomic gas is confined to some of the loops in the outskirts of the main body and to the tidal tails. The model-subtracted *B* imaged emphasizes the faint shells and loops around the body, and suggests the continuation of the NW tail across the face of the remnant to the south–southeastern loop (from point A to B). (d) A *B*−*R* color map in negative greyscale, along with the same H I column density contours as in (c). The colors range from *B*−*R*=1.2 mag (white) to *B*−*R*=1.6 mag (black). The center of the remnant and a bright star just to the northeast of point C appear white due to saturation of the *R*-band CCD image. The color map is noisy near its edges where the *B* and *R* surface brightnesses approach zero and areas outside the remnant body have been blanked (white). Color measurements at the points labeled A—M are listed in Table 5. The dust lane indicated by the red ridge south of points B–D imply that the NW tail crosses the face of the remnant. The bluer colors of the south–southeastern and W loops (points H–I and J–L) support the idea that they are the continuations of the blue NW (points A–C) and E (point M) tidal tails, respectively. No correction has been made for contamination by Hα line emission in the *R* band which may be responsible for the red *B*−*R* colors in the central region. (e) The blue optical continuum image in negative greyscale with regions containing x-ray emission greater than 3σ above the background set white. The solid contours within this region map the Hα emission while the dashed contours map the atomic hydrogen column density [same levels as in (c)]. In contrast to the atomic gas, the warmer gas phases are centrally concentrated. The warm ionized gas extends, at least in projection, out to the atomic hydrogen contours. (f) The contours map the molecular-gas disk imaged by WSS; the extent of the Hα line emission is shown by the central white area (changing to light-grey where the Hα and H I emission overlap at intermediate radii); and the outer deep-grey tone encompasses regions with an H I column density above 7.5×10^{19} cm^{-2}. The optical *B*+*R* sum image (continuous negative greyscale) is in the background. The contours are at molecular hydrogen column densities of (1, 2, 3, 4, 5) $\times 1.25\alpha_{CO}10^{22}$ cm^{-2}. There is a prominent gap between the cold molecular and atomic gas components in the main body (WSS) that is filled in by warm ionized gas.
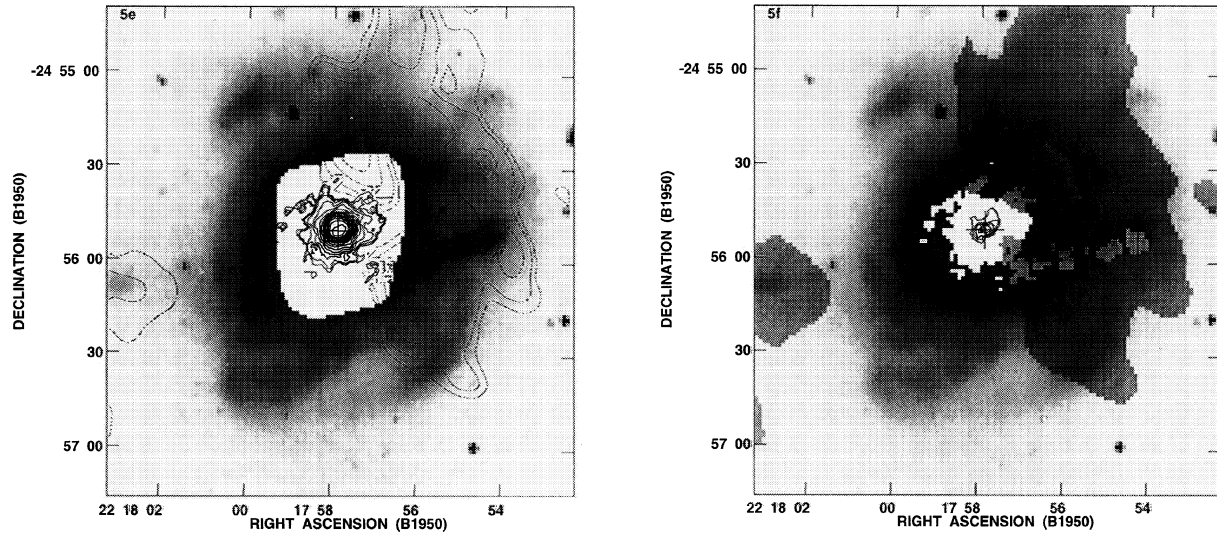
FIG. 5. (continued)

the white areas on the outside of the main body have deliberately been set to zero.

The observed $B-R$ colors lend support to the geometry proposed earlier in this section, particularly the contention that the NW tidal tail lies in front of the remnant. In the region where this tail crosses the face of the galaxy, a red ridge and a deep furrow in the optical light distribution [particularly in the B band; see Figs. 5(b) and 5(c)] indicate the presence of a dust lane lying just south of the center line of the tail. Clearly, this dust concentration is associated with the NW tail and is seen in absorption against the background light from the galaxy. The reddest point of the dust lane lies very close to and just below a peak in the H I column density, and the lane crosses the remnant diagonally from NW to SE.

Surface brightness and color measurements of the points labeled A–M in Fig. 5(d) are listed in Table 5. The color at the apparent base of the NW tail is quite blue [$B-R = 1.20$ at point A in Fig. 5(d)] but becomes progressively redder as the tail crosses in front of the main body through points B and C ($B-R = 1.30$ and 1.34, respectively). This trend in color is likely due to the decreasing ratio of surface brightnesses of the blue tail to the red remnant body as one moves inward along the tail. The portion of the E tail seen at the left edge of Fig. 5(d) (point M) has $B-R = 1.16$. The main body of the remnant is significantly redder with $B-R \approx 1.38$ (points D–G). The south–southeastern loop (points H and I) is bluer than the remnant body, with some regions as blue as parts of the W loop (points J–L), supporting the idea that these loops are the continuations of the blue NW and E tidal tails, respectively.

The fact that the southern leg of the W loop is brighter [Fig. 5(c)] and somewhat bluer [point J in Fig. 5(d)] than the northern leg, and the fact that Hα line emission is only seen along the southern leg might suggest that the northern leg lies behind the (obscuring) remnant body. However, the optical morphology of this central region [Fig. 5(c),

S82] suggests exactly the opposite: That the W loop emerges from behind the galaxy in its southern leg, a continuation of the E tail, and wraps around to the foreground in its northern leg. In this case, both the blue colors and enhanced optical brightness of the southern leg may be a result of the vigorous star formation seen in this feature. We prefer the latter orientation, since that connects the W loop to the E tail more naturally, but the present data do not allow us to unambiguously discriminate between the two possibilities.

Figure 5(e) is a combination of the data from the first three panels [Figs. 5(a)–5(c)]. The B image is shown again in negative greyscale, but with regions containing x-ray emission greater than 3σ above the background set white. Within this region, the solid contours map the Hα emission. The atomic hydrogen distribution is indicated by dashed contours. The H I extends up to the ionized gas

TABLE 5. Colors in main body of NGC 7252.

Region	μ_B (mag arcsec^{-2})	$B-R$[a] (mag)
A	23.8	1.20 ± 0.02
B	23.4	1.30 ± 0.02
C	22.7	1.34 ± 0.01
D	22.6	1.39 ± 0.01
E	21.5	1.38 ± 0.01
F	21.5	1.39 ± 0.01
G	21.6	1.35 ± 0.01
H	23.7	1.30 ± 0.02
I	23.9	1.27 ± 0.02
J	23.1	1.33 ± 0.01
K	22.6	1.23 ± 0.01
L	23.8	1.27 ± 0.02
M	24.6	1.16 ± 0.03

Notes to TABLE 5

[a]The 1σ color errors are based on the sky noise levels in the B and R images.

contours, at least in projection. Following a path approaching the main body along the ridge of the NW tail, the H I column density drops by over a factor of 6 from a peak value of 2.8×10^{20} cm^{-2} to less than 5×10^{19} cm^{-2} over a projected distance of only $12'' \approx 2.8$ h^{-1} kpc.

Finally, Fig. 5(f) includes a map of the molecular gas, illustrating the relationship between the cold and warm gas phases: the contours show the ^{12}CO($1 \rightarrow 0$) gas disk imaged by WSS; the extent of the Hα emission is indicated by the central white area (turning light-grey where Hα and H I emission overlap at intermediate radii); and the outer deep-gray tone marks the region covered by the H I. The continuous (negative) greyscale image in the background shows the starlight in the form of the optical $B+R$ sum image. There is a prominent gap between the molecular and atomic gas components in the main body (WSS). Figure 5(f) shows that this gap is filled in by warm ionized gas.

We use these data to investigate the cold gas content of the merger remnant. Assuming that the H I column density at the center of the main remnant body is less than 5×10^{19} cm^{-2}, the Swedish–ESO Submillimeter Telescope measurements of Dupraz *et al.* (1990) place a lower limit to the ratio of molecular to atomic gas column densities of $N_{\mathrm{H_2}}/N_{\mathrm{H\,I}} > 40$ α_{CO} within $r < 22''$. The conversion factor α_{CO} in the above equations, relating the integrated ^{12}CO($1 \rightarrow 0$) emissivity to the molecular hydrogen column density, is estimated to be about 0.5–1.5 (Maloney 1989). The ^{12}CO($1 \rightarrow 0$) flux measured by WSS within $r < 7\farcs5$ is about three-quarters of that found by Dupraz *et al.* (1990) using a much larger beam ($r = 22''$), indicating that the molecular gas is quite centrally concentrated.

The elliptical model that has been fit to the B-band image [in order to create the residual image shown in Fig. 5(c)] yields the azimuthally averaged blue surface brightness as a function of radius. Ellipse fitting is done in two ways: In one case, regions around bright stars, prominent tidal features (loops, shells, and tails), and the dust lane are excluded from the fit, while only stars are masked out in the second case. The R image has been analyzed in a similar fashion and the resulting brightness profile is plotted in Fig. 6 as a function of the fourth root of the radius. A de Vaucouleurs $r^{1/4}$ law (de Vaucouleurs 1953) is a straight line in this diagram and is quite a good approximation to the brightness profile of the main body of NGC 7252. Figure 6 shows that the R-band profile is not very sensitive to the details of masking. The B profile also resembles an $r^{1/4}$ law, though to a lesser degree than the R profile. This is probably due to the increased prominence of the blue loops and the dust lane in the B image. The de Vaucouleurs law that best fits the R data has an effective radius $r_e = 14'' \sim 3.3$ h^{-1} kpc and an effective surface brightness $\mu_{e,R} = 20.2$ mag arcsec^{-2}. These values are similar to those derived for ellipticals (see Sec. *4.4* for a discussion).

3.2.2 Kinematics

The data of WSS show that the molecular- and ionized-gas disks in the center of NGC 7252 display very similar
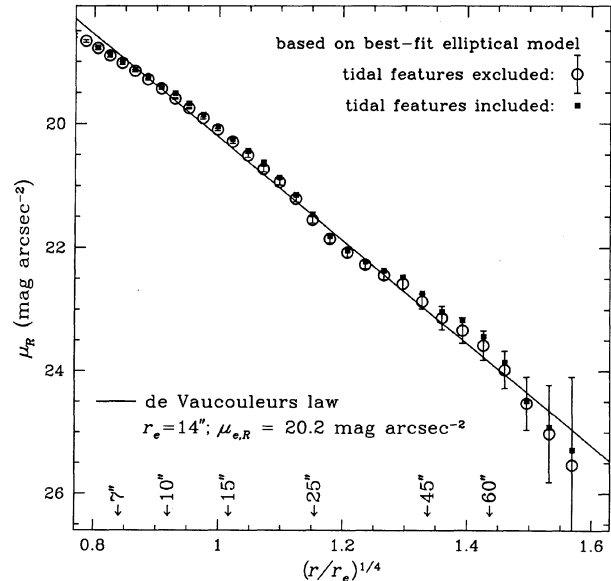

FIG. 6. Radial light distribution of the NGC 7252 remnant: R surface brightness as a function of the fourth root of radius (in units of the effective radius $r_e = 14''$). The brightness profile is derived by fitting ellipses to the isophotes (see Sec. *3.2.1*). The open circles and 1σ error bars represent a fit excluding bright stars, prominent tidal features, shells, and the dust lane, while the filled squares show a fit in which only the stars are excluded. The profile is well approximated by a de Vaucouleurs $r^{1/4}$ law (straight line) that is characteristic of elliptical galaxies.

kinematics (see Fig. 6 of WSS). The CO velocities seem to fill in the missing central parts of the Hα rotation curve, and extend out to what WSS refer to as the "turn-over" in the Hα rotation curve at $\sim 5''$ radius. Beyond this radius, the ionized gas exhibits unusual motions, such as velocity reversals along the major axis and large velocities along the minor axis (S82).

Figure 7 compares the kinematics of the atomic and ionized gas near the center: the tickmarks along the major axis (position angle $\sim 116°$ E of N) and minor axis of the inner gas disk show the Hα velocities at $2\farcs3$ intervals (from S82), while the open contours display the intensity-weighted mean H I velocity field. The background grey-scale image in Fig. 7 is the $B-R$ color map, with red $B-R$ colors as dark tones (and vice versa), and the islands of white pixels show the region covered by the Hα emission. The central Hα contours (at the location of the cross) indicate the orientation of the inner ionized-gas disk.

The Hα velocities from $r = 10''$ to $20''$ along the minor axis agree quite well with those of the H I, especially near the apparent base of the NW tail. The red $B-R$ colors in this area, north of center, are due to the dust lane (associated with the NW tail) crossing the face of the galaxy. The similarity between the kinematics of the H I and Hα (and between the morphologies of the Hα emission and dust lane) suggest that the Hα emission in this region may be associated with this dust lane. Similarly, the velocity of the ionized gas between $r = 10''$ and $25''$ along the southwestern half of the minor axis has the same sign and ap-
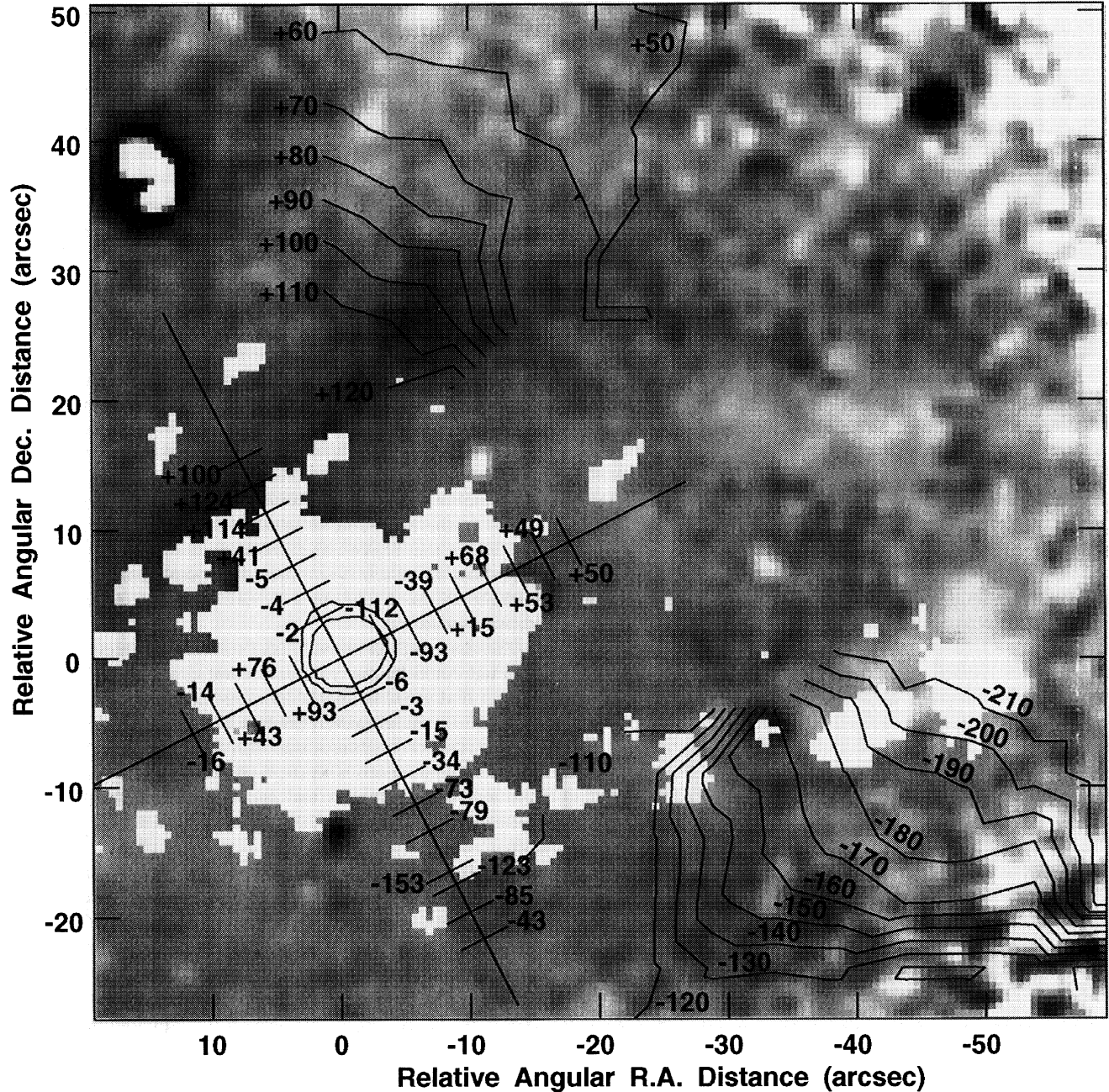
Greyscale range: B-R = 1.2 to 1.8
Hatched Cross+Numbers = H-alpha Slit Position and Velocities From S82

FIG. 7. A detailed comparison between the $H\alpha$ kinematics of the central ionized-gas disk and the H I kinematics at the base of the NW tail and in the W loop complex. The greyscale is a $B-R$ color map of the remnant [as in Fig. 5(d)], but with regions of $H\alpha$ emission set white. North is up and east is to the left. The tickmarks along the major axis (position angle: 116° E of N) and minor axis of the inner gas disk show the $H\alpha$ velocity measurements of S82 at 2".3 intervals. The inner ionized-gas disk is indicated by the closed contours at the central cross. The outer open contours show the kinematics of the H I. All velocities are in km s^{-1} relative to systemic. The H I velocities at the base of the NW tail associated with the dust lane [see Fig. 5(d)] and in the W loop complex containing a chain of H II regions match up approximately with the high positive and negative $H\alpha$ velocities along the northeastern and southwestern semiminor axes, respectively.

proximate magnitude as the velocities of the H I in the W loop. This southwestern minor axis Hα emission appears to be the natural continuation of the Hα emission in the W loop with which the H I in this region is associated. Thus, the strong Hα motions observed beyond 10" on the minor axis probably originate from gas which is kinematically and spatially separated from the inner gas disk, and which is more likely associated with the tidal tails and loops. It is the combination of these two different kinematical systems that gives rise to the observed minor axis velocity profile measured by S82. The detected H I is not obviously related (spatially) to the ionized gas along the major axis, so it is not possible to draw direct conclusions about the observed major-axis countermotions.

In conclusion, the spatial and kinematic separation between the atomic and molecular gas suggests that all of the detected neutral hydrogen lies outside the main body of the remnant. There are at least two distinct components of ionized gas: one associated with the inner rotating molecular-gas disk and one associated with the tidal features (tails and loops).

3.3 Gas and Star Formation in the Tidal Tails

3.3.1 Large scale properties of stars and gas

Optical *B*- and *R*-band CCD mosaic images have been used to study the $B-R$ color distribution in NGC 7252. In the present study, we consider only the relative $B-R$ colors of different parts of this galaxy, postponing a more detailed analysis of the colors to a future paper. The main results are: (1) the tidal tails are 0.2–0.5 mag bluer in $B-R$ than the outer regions of the main remnant body; and (2) the bluest colors tend to occur at regions of peak optical and H I emission in the tidal tails (i.e., at the H II regions) and in the W loop.

The very blue knots associated with Hα+[N II] emission are undoubtedly regions with young stars that have ionized the surrounding interstellar medium. In regions with blue $B-R$ colors but *no* associated Hα+[N II] emission, such as the blue ridge at the apparent base of the NW tail (see Sec. *3.2.1*), the presence of a hot, young stellar population is not quite so obvious. Wavelength-dependent extinction by dust that is mixed in with either the stars or the atomic gas in the tidal tails may cause color differences, but the effect expected is opposite that observed—dust should cause the starlight near the light and gas peaks to appear redder, not bluer. A contrived (low) metallicity distribution in the tails could be responsible for part of the observed blueing trend. However, the most natural explanation for the blue $B-R$ colors is that the stellar populations in the tidal tails are younger than those in adjacent regions in the main body of the galaxy. This conclusion agrees with the results of a study of 25 Arp systems by Schombert *et al.* (1990) in which it was found that the blue colors in the tidal features were caused primarily by star formation.

In order to measure the relative amounts of optical starlight associated with the different tidal features and the main body of NGC 7252, stars are removed from the

B-band image using DAOPHOT and the best-fit elliptical model is subtracted [see Sec. *3.2.1* and Fig. 5(c)]. The resulting residual image is then convolved with a circular Gaussian of FWHM=15" to match the resolution of the C-array H I data. This yields a low-resolution, but deep optical image reaching $\mu_B = 27$ mag arcsec^{-2}. The blue luminosities L_B of various components are listed in Table 4, together with their H I mass-to-blue light ratios $\mathcal{M}_{HI}/L_B$.

The tidal features and "fine structure" contain ~13% of the total blue luminosity: The NW tail contributes 5%, the E tail ~2%, the W loop another 2%, and the remaining loops, shells, and ripples near the remnant contribute ~4%. The remaining ~87% of the light comes from the smooth component of the main body as estimated from the best-fit model.

The smoothed optical image shows that the surface brightness of the optical tails falls off just beyond the H II regions, with material of lower surface brightness extending ~50"≈12 h^{-1} kpc beyond the H II regions in both tails. In the NW tail, the drop in surface brightness at that point is very sharp, and there is no optical equivalent to the H I which reaches at least 40 h^{-1} kpc beyond the optical cutoff. In the E tidal tail, the optical emission fades gradually into the background without any sharp drop in brightness. More sensitive observations may reveal that the starlight in the E tail does indeed extend as far as the atomic gas does.

The sharp fall-off in the optical surface brightness of the NW tail could be due to a projection effect, if the tail is bent at that point so that it happens to be oriented along our line of sight. However, the fact that the neutral hydrogen distribution continues smoothly past the break in the optical tail, combined with the fact that the H I isovelocity contours are continuous and evenly spaced through this feature [Figs. 4(a) and 4(b)], argues against this possibility.

The H I emission in both tidal tails is mostly spatially resolved with approximately the same (angular) width as the blue light. A comparison of the VLA C-array H I image and the cleaned, smoothed *B*-band image shows that the atomic hydrogen is distributed like the stars within the boundaries of the optical tails. The average optical width (FWHM) is 16.6"±3.4"≈3.8±0.8 h^{-1} kpc along the E tail, and a surprisingly constant 26.6"±1"≈6.1±0.2 h^{-1} kpc along most of the NW tail.

By contrast, there are spatially unresolved knots of H I around the main body of NGC 7252: (1) near the apparent base of the NW tail, where the peaks of the gas distribution lie along a bright ridge of starlight, coincident with areas of blue $B-R$ color [regions A and B in Fig. 5(d)]; and (2) in the W loop, where the most prominent unresolved clump of H I lies close to the brightest westernmost H II region, which is also very blue in $B-R$ [point K in Fig. 5(d)].

3.3.2 Giant H II regions

The gas and stellar distributions in the tidal tails show a considerable amount of correlated spatial structure: Each optical condensation is accompanied by a nearby H I peak,

and these are invariably the ones with the highest gas column density ($N_{H\,I} \gtrsim 2 \times 10^{20}$ cm^{-2}). The most striking examples are the giant H II regions near the end of each optical tail. The fact that the atomic gas displays smooth continuity across these H II regions, both morphologically and kinematically [see Fig. 4(b)], argues that the clumps of H I seen near these star-forming regions are physically associated with them and represent actual enhancements in the gas density and velocity dispersion (see below). These H I knots are *not* mere artifacts of viewing geometry.

Figures 8 and 9 show details of the NW and E tails, respectively, in the vicinity of the H II regions: panels (a) contain the $B+R$ sum image in (negative) greyscale, with islands of white marking the extent of the Hα emission, and with H I contours overlaid; panels (b) show the $B-R$ color map in greyscale (red colors indicated by dark-grey tones and vice versa) and contours of the H I column density; and panels (c) show the spatial distribution of the 1σ line-of-sight velocity dispersion of the H I in (negative) greyscale, derived from the C-array data cube, with H I column density contours superimposed. Table 6 lists some observed properties of the atomic gas and starlight along each tidal tail, measured in the regions delineated by the boxes in Figs. 8(c) and 9(c). Table 7 summarizes the observed characteristics and derived physical properties of the two giant H II regions.

It is clear from these figures and tables that each of the H I regions is associated with large amounts of H I, comparable to the mean total H I content of dwarf irregular galaxies (Hunter & Gallagher 1985). The column density of this H I exceeds that of the gas in the surrounding tail by factors of 2–3. Further, the $B-R$ color becomes progressively bluer toward each H II region, despite the fact that the R-band flux is contaminated by Hα line emission. Figure 8(a) shows two stellar objects near the NW H II region: one projected onto the tail about 10″ to the north–northwest of the H II region, and another off the tail about 30″ to the southwest. These are known to be foreground stars (Schweizer 1993) and we have subtracted a scaled point spread function from each using DAOPHOT before measuring the optical parameters of this H II region. However, the proximity of the north–northwestern star to the Hα centroid implies that the optical luminosity and color measurements of this H II region are quite uncertain due to possible errors in the subtraction of this star.

Since the H I velocity distributions are single valued along the tails [i.e., the spectrum at each point has a single peak as seen in Fig. 4(b)], their linewidths are well defined. Figures 8(c) and 9(c) show that each tail has a local maximum in the line-of-sight velocity dispersion near the H II regions. In the NW tail, the dispersion has a maximum exactly at the position of the H II region [marked by a cross in box C in Fig. 8(c)] and falls off symmetrically on either side. The peak linewidth (FWHM) is 30% or 10 km s^{-1} higher than the mean value for the tail. In the E tail, the H II region [the cross in box F in Fig. 9(c)] does have a larger H I linewidth than the mean along the tail, but the maximum dispersion occurs 25″ to the west at a local minimum in the H I column density [box D in Fig.

9(c)] where the gas distribution becomes narrower. This local minimum in both the atomic gas column density and optical surface brightness argues against (but does not exclude) the large linewidth here being due to an increase in the path length along the line of sight.

The giant H II region of the NW tail has an Hα diameter (full width at zero intensity) of 1.9 h^{-1} kpc, which is comparable in linear extent to the largest of the giant H II regions seen in external galaxies (see the reviews by Kennicutt 1984; Hodge 1993). The comparison is limited to their linear sizes, however, since our Hα measurements of NGC 7252 are not photometrically calibrated. The peak in the Hα+[N II] emission coincides in position with those in the H I column density and velocity dispersion and with a region of very blue $B-R$ color. Further, the spatial distributions of gas column density, H I linewidth, and optical $B-R$ color are symmetric about the NW H II region. The H I mass within the FWHM of the associated H I clump is an enormous 1.6×10^8 $h^{-2} \mathcal{M}_\odot$ and the blue luminosity within the same area is 1.9×10^8 $h^{-2} L_\odot$, yielding a $\mathcal{M}_{H\,I}/L_B$ of $0.8 \mathcal{M}_\odot/L_\odot$, which is the same as that derived for the NW tail as a whole.

Although the giant H II region of the E tail is similar to the one in the NW tail in its global properties, it is different in detail. The Hα emission is barely spatially resolved (diameter $\sim 3\rlap{.}''5 \approx 0.8$ h^{-1} kpc), and the total Hα line flux is only 10% that of the NW region. This H II region has the bluest $B-R$ color of any area in NGC 7252. The underlying stellar condensation in the E region, all of which is blue in color, appears to be more spread out (FWHM ~ 1.6 h^{-1} kpc) and of lower luminosity ($L_B = 1.0 \times 10^8$ $h^{-2} L_\odot$) than in the NW. The maximum in the H I column density does not coincide exactly with that in the Hα or with any peak in the optical continuum, instead falling $\sim 10''$ to the east of the Hα peak. As with the starlight, the H I at the location of the E region is distributed over a larger area than in the NW H II region, with an H I mass of 1.4×10^8 $h^{-2} \mathcal{M}_\odot$ within the FWHM of the 21 cm line emission (6 h^{-1} kpc $\times 3$ h^{-1} kpc). The gas mass to blue light ratio of the E H II region is unusually high, but similar to the value of $\mathcal{M}_{H\,I}/L_B = 1.3$ $\mathcal{M}_\odot/L_\odot$ derived for the E tail as a whole.

4. DISCUSSION

An extensive set of observational data on the gas phases and starlight in NGC 7252 has been presented in the preceding sections. We discuss here what these data might be telling us about the consequences of the recent merger in this system and the future evolution of the remnant. This section is organized as follows: Sec. *4.1* comments on the nature of the two progenitor galaxies based on the properties of the gas and starlight in the system; Sec. *4.2* discusses the observed kinematics in the light of previous modeling efforts; Sec. *4.3* investigates why the remnant body is so devoid of H I; Sec. *4.4* considers whether the present remnant will resemble an elliptical galaxy more closely in the future; and Sec. *4.5* investigates whether the clumps in the tidal tails are bound units.
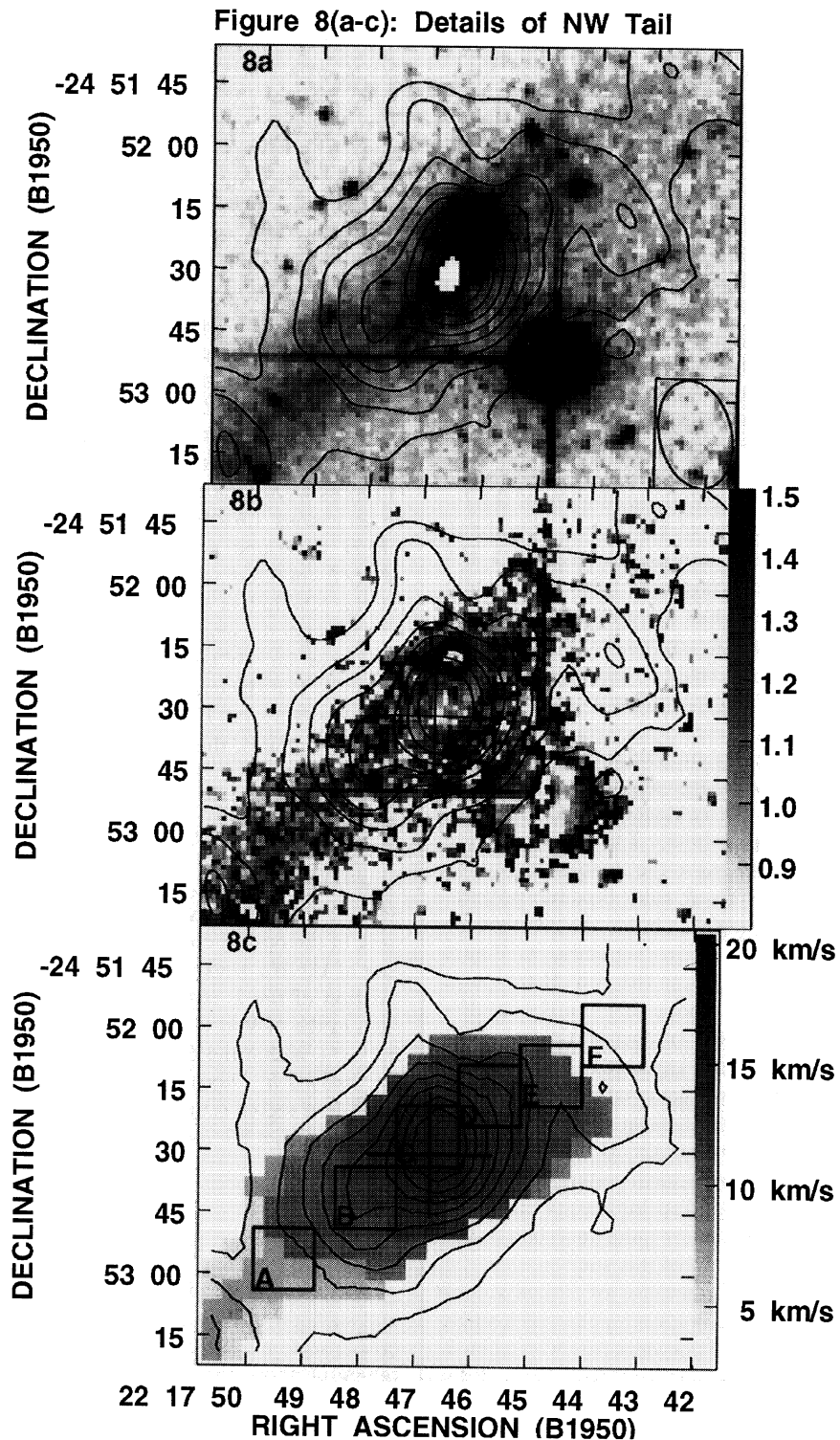
Figure 8(a-c): Details of NW Tail

FIG. 8. Details of the NW tail and giant H II region (marked by a cross). (a). The *B*-band light (negative greyscale) and Hα line emission (white pixels). The contours show the H I line emission (C+D data) at column density levels of (7.5, 10, 15, 20, 25, 30, 35, 40) $\times 10^{19}$ cm^{-2} and the beam is shown at lower right. Two foreground bright stars, one only ~10″ to the north–northwest of the H II region, make any optical measurements of this region uncertain. (b) A $B-R$ color map of this region in negative greyscale (vertical bar is in magnitudes), with H I column density contours as in (a). The central portions of both nearby stars are saturated. (c) The spatial distribution of the rms H I line-of-sight velocity dispersion (second moment of C-array data cube) in negative greyscale, with overlaid H I column density contours (C+D data) as in (a). Optical and H I measurements at the locations of the boxes labeled A–F are listed in Table 6. The peaks in the H I column density, Hα emission, $B-R$ colors, and H I linewidth are all coincident. The large quantity of neutral hydrogen, the blue luminosity, and the linear size of this region are similar to that of a dwarf galaxy.

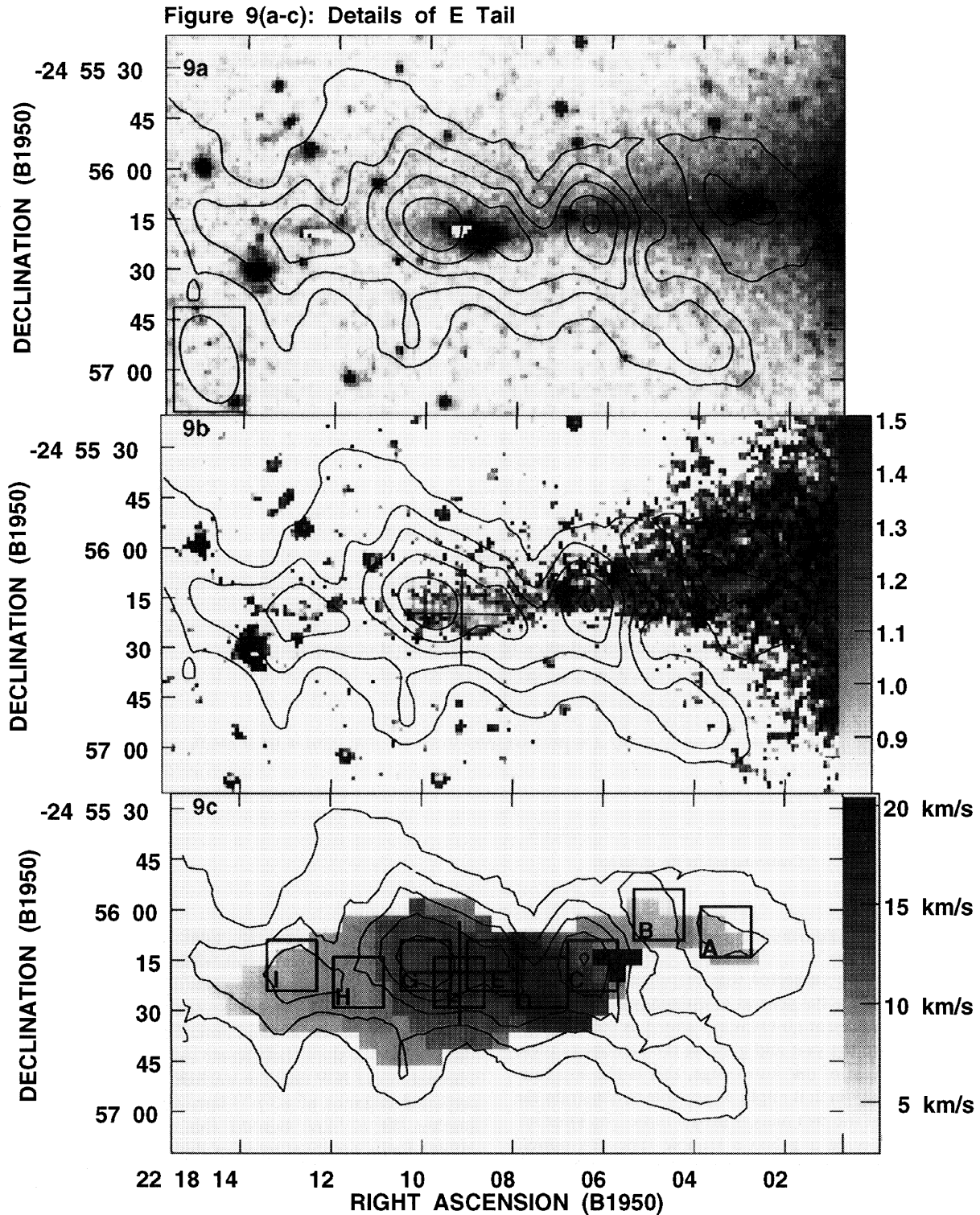**Figure 9(a-c): Details of E Tail**

FIG. 9. Details of the E tail and giant H II region (cross), at the same scale as Fig. 8. (a) Same as Fig. 8(a) for the E tail. (b) Same as Fig. 8(b) for the E tail. (c) Same as Fig. 8(c) for the E tail. Optical and H I measurements at boxes A–I are listed in Table 6. The area of bluest $B-R$ color is centered on the Hα emission in the giant H II region, but the peak in the H I column density is offset 10″ to the east, and the region with the largest H I linewidth is displaced 25″ to the west.

TABLE 6. Properties along tails.

(1) Area	(2) Distance (h^{-1} kpc)	(3) V_{HI} (km s^{-1})	(4) ΔV_{HI} (km s^{-1})	(5) N_{HI} (10^{20} cm^{-2})	(6) μ_B (mag arcsec^{-2})	(7) $B - R$ (mag)
NW Tail						
A	48	−45	18	0.9	26.0	1.15±0.04
B	54	−52	27	2.6	26.0	1.10±0.05
C[a]	59	−60	31	4.0	25.0[b]	1.00±0.03[b,c]
D	63	−63	27	2.4	25.0[b]	1.34±0.02[b]
E	66	−62	23	1.3	26.2	1.33±0.05
F	70	−59	18	0.9	∼27	−
E Tail						
A	18	+9	16	1.0	24.9	1.15±0.02
B	23	+23	17	0.4	25.3	1.30±0.03
C	28	+41	34	2.1	25.7	1.22±0.03
D	31	+57	38	1.9	26.4	1.17±0.06
E	34	+74	35	2.1	24.4	0.88±0.05
F	37	+77	31	2.3	24.0	0.95±0.05[c]
G[a]	39	+82	29	2.6	25.1	1.02±0.05
H	44	+88	21	1.5	∼27	−
I	48	+91	18	1.6	∼26.5	−

Notes to TABLE 6.

(1) Region of measurement, as delineated by the boxes in Figures 8c and 9c.

(2) Projected distance of region from remnant center.

(3) Radial velocity of H I relative to systemic (4740 km s^{-1}, WSS), measured from the C-array data.

(4) FWHM of 21 cm line, based on fitting a gaussian profile to the C-array data.

(5) H I column density from C+D array data.

(6) *B*-band surface brightness.

(7) $B - R$ color and 1σ errors. The latter are based on the sky noise levels in the *B* and *R* images.

[a] Location of H I clump.

[b] Uncertain due to proximity of bright star.

[c] Contaminated by Hα emission.

4.1 Gas Distribution and Progenitors

It has long been suspected that two disk galaxies were required to produce the general morphology of NGC 7252 (TT;S78). The present observations afford us the opportunity to peer into the past and glimpse the identity of these disks. To the best of our knowledge, this is the first late-stage merger for which it might be possible to constrain the Hubble types of the two merger progenitors. The information used to decide a galaxy's Hubble type—its optical morphology (nature of spiral arms, bulge-to-disk ratio, etc.)—is impossible to come by for merged galaxies like NGC 7252. Only the outer parts of the progenitor galaxies might conceivably have retained their identities, having been stretched into tidal tails (see Fig. 15 of TT). The amount of distribution of atomic gas in the outer parts of galaxies varies across the Hubble sequence and this may be used as a secondary criterion for the classification of the progenitors.

The H I content of the tidal tails in NGC 7252 ($\mathcal{M}_{HI}/L_B \sim 1$) is consistent with that seen in the outer parts of late-type, gas-rich spirals (Wevers *et al.* 1986). The most notable difference between the two tails is in the relative extents of the H I and optical distributions: The gas and starlight in the E tail appear to have the same extent, whereas in the NW tail, the starlight cuts off sharply at a projected distance of 80 h^{-1} kpc, while the H I extends another 40 h^{-1} kpc beyond this point. Cayatte *et al.* (1994) find a marginal trend in the ratio of optical to H I diameters across Hubble types indicating that the E tail progenitor might be an earlier-type spiral than the NW tail progenitor.

4.2 Kinematic Structure of the Tidal Features

The H I at the apparent base of the NW tail is seen to be moving away from us with velocities in excess of 100 km s^{-1} relative to the nucleus, while the rest of the NW

TABLE 7. Properties of tail clumps.

Quantity	NW Region	E Region	notes
Measured Properties of Ionized/Atomic Gas:			
Projected distance of H I clump (h^{-1} kpc)	59±2.0	39±2.0	
Projected distance of H II region (h^{-1} kpc)	58±0.5	36±0.5	
Relative radial velocity of H I clump (km s^{-1})	−60±3	+82±3	[a]
Relative radial velocity of H II region (km s^{-1})	−83±15	+74±15	[b]
Peak H I column density (10^{20} cm^{-2})	5.5	3.2	[a]
FWHM of H I line (km s^{-1})	31	29	[a]
$r_{\rm HI}$ (h^{-1} kpc)	3.6×3.3	6.0×3.1	[c]
$M_{\rm HI}(r_{\rm HI})$ ($10^8 h^{-2} M_\odot$)	1.6	1.4	[d]
Measured Optical Properties:			[e]
$L_B(r_{\rm HI})$ ($10^8 h^{-2} L_\odot$)	1.9	1.0	[f]
$(M_{\rm HI}/L_B)_{r_{\rm HI}}$ ($M_\odot/L_\odot$)	0.8	1.4	
r_B (h^{-1} kpc)	0.5×0.4	1.6×0.9	[g]
$L_B(r_B)$ ($10^7 h^{-2} L_\odot$)	3	4	[h]
$B-R$	1.00	0.88	
Derived Parameters:			
$M_{\rm virial}$ ($10^8 h^{-1} M_\odot$)	11	15	[i]
$M_{\rm HI}/M_{\rm virial}$ (h^{-1})	0.30	0.20	[j]
$M_{\rm gas}/M_{\rm virial}$ (h^{-1})	0.38	0.26	[j]
$M_{\rm virial}/L_B$ ($h M_\odot/L_\odot$)	3.0	7.3	[k]
$M_{\rm tidal}$ ($10^8 h^{-1} M_\odot$)	1.5	2.1	[l]
$M_{\rm HI}/M_{\rm tidal}$ (h^{-1})	2.1	1.3	

Notes to TABLE 7

[a] Measured from C-array data cube.

[b] From Schweizer (1982).

[c] Deconvolved semimajor and semiminor axes (0.5×FWHM) of the H I brightness distribution.

[d] H I mass within $r_{\rm HI}$.

[e] Uncertain for NW region due to proximity of bright star.

[f] B-band luminosity within $r_{\rm HI}$.

[g] Semimajor and semiminor axes (0.5×FWHM) of the blue light distribution.

[h] B-band luminosity within r_B.

[i] Virial mass (see Sec. 4.5 for a discussion).

[j] The total H I mass is $2 \mathscr{M}_{\rm HI}(r_{\rm HI})$ since $r_{\rm HI}$ encloses half the total mass for a two-dimensional (2D) Gaussian distribution. The total gas mass corrects the total H I mass for the cosmic He abundance. A ratio of unity indicates that the H I (or gas) alone can account for the binding mass of the system inferred from its velocity dispersion.

[k] The total B luminosity is $2L_B(r_B)$ since r_B is the half-light radius of a 2D Gaussian distribution.

[l] The mass required to prevent tidal disruption (See Sec. 4.5), calculated assuming a remnant mass of $3\times10^{11} h^{-1} \mathscr{M}_\odot$ and a radius of $r_{\rm HI}$ for the H II region.

tail is swinging toward us (Sec. 3.1.2). Both the morphologies of the NW tail and south–southeast loop (S82) and our color data suggest that the NW tail crosses in front of the main body. If the NW tail is a continuous structure, as suggested by Fig. 4, the individual gas clouds of the tail that are moving at velocities higher than systemic must follow rather noncircular orbits and must presently be on their way in to smaller radii, having passed through the apocenter of their orbits. Only in this way can this material have the same sense of angular momentum as the more distant tidal tail and yet be redshifted.

We also find that the H I velocities of both the W loop and the NW tail agree in sign and approximate magnitude with the H II velocities measured by S82 near the same regions (Sec. 3.2.2). This suggests that the H II gas beyond the central disk may be associated with tidal features, moving on noncircular orbits. The superposition of the line-of-sight motion of such foreground clumps of ionized gas and the rotational motion of the central ionized-gas disk might be responsible for the appearance of nonzero motions along the minor axis, and might conceivably explain the major-axis velocity reversals. Thus, all of the observed H I, H II, and ^{12}CO(1→0) may belong to kinematic structures that have their angular momentum vectors pointed in roughly the same direction.

The returning tidal material from the NW tail may help explain some of the prominent morphological features of the NGC 7252 remnant: the numerous shells and ripples seen in Fig. 5(c) [see also Fig. 2(d) of S82]. Numerical simulations of equal-mass mergers suggest that cold material from the tidal tails falling back into a remnant lead to the continued formation of such ripples or shells (Barnes 1988, 1992; Hernquist 1992; Hernquist & Spergel 1992). The direct kinematical evidence for tail gas falling toward the remnant in the present observations strongly supports this prediction.

The previous numerical simulations of this system (Borne & Richstone 1991; Mihos et al. 1993) managed to match the approximate velocities of the tail H II regions measured by S82. However, the rest of the tail velocities in these simulations have exactly the *opposite* behavior to that observed [see Figs. 4(a) and 4(b)]: starting from the NW/E H II region, the simulation velocities become more and more negative/positive as one moves to smaller radii (see Fig. 10 of Borne & Richstone 1991; Fig. 23 of Mihos et al. 1993). The encounter in the simulations also required a very close, short-period orbit, with the galaxies actually in contact even at apocenter, and resulted in the encounter being a recent event, not allowing enough travel time for the tails to reach their presently observed positions. These numerical solutions were driven to a retrograde encounter geometry (i.e., the spin of the progenitors' disks opposite to their mutual orbital motion) in order to match the velocity reversals observed along the minor axis (Borne & Richstone 1991).

We propose that a prograde encounter geometry may reproduce both the observed tail kinematics and the velocity reversals in NGC 7252. Since a prograde encounter affects the disk material sooner and more strongly than a retrograde one (TT), it should allow a wider, longer-period encounter, giving the tails more time to reach their present lengths. The longer times resulting from the more distant encounter may also allow the inner tidal material enough time to reach apocenter and turn around, giving rise to the observed velocity reversals. Only a full modeling effort can test this hypothesis.

4.3 Dearth of Central Atomic Gas

The idea that galactic mergers tend to deposit large amounts of gas into the central regions is one that is supported by both observational and theoretical investigations. It may therefore be somewhat surprising that we do not detect any H I in the main body of the remnant. As discussed in Sec. 4.1 above, we expect the progenitors to be late-type spirals. Such galaxies typically have lower ratios

of molecular to atomic gas column densities, even in their central regions, than that found here (for the ratio in spirals, cf. Young 1989, and references therein; for the NGC 7252 remnant, see Sec. *3.2.1*). We therefore conclude that the central neutral atomic hydrogen has been radically rearranged by the merger. In addition, the kinematics suggest that H I gas is moving to smaller radii from the tidal regions at the apparent base of the NW tail (Sec. 3.1). The fact that this gas disappears rather abruptly, whereas the optical tail continues past the face of the galaxy (Sec. 3.2), suggests that there may be an efficient, quick, and ongoing process converting the returning atomic gas to other phases within the remnant body. The observations point to several likely sinks for the central atomic gas: It may be compressed into molecular gas, some of which may in turn be converted into stars, and it may be heated into warm ionized hydrogen or a hot, x-ray emitting plasma.

The molecular-gas disk imaged by WSS may have been produced by the first of these mechanisms. This disk reaches a peak surface density of 1120 α_{CO} $\mathcal{M}_\odot$ pc^{-2}, and accounts for 33 h^{-1}% of the dynamical mass within a 1.1 h^{-1} kpc radius. The centrally concentrated molecular gas distribution seen in NGC 7252, a late-stage merger remnant, is similar to that in ongoing mergers (Sanders *et al.* 1988; Scoville *et al.* 1989,1991), but very different from the distribution in isolated spirals (Kormendy & Sanders 1992). However, NGC 7252 differs from systems in less advanced stages of merging in that the *amount* of molecular gas and infrared luminosity are not increased over isolated spirals of similar blue luminosity (compare the values in Table 4 with Young *et al.* 1986; Solomon & Sage 1988; Braine & Combes 1993). Note that the relatively high molecular gas masses inferred for ongoing mergers may instead be due to the use of a different conversion factor between CO and H_2 than that derived for the Galaxy (Maloney 1989). The "normal" molecular gas content and infrared luminosity of NGC 7252 suggests that, if the efficiency of molecular cloud formation is increased at some point during the merger, some other process—such as efficient star formation—brings it back down to normal levels in a reasonably short time.

The possibility that a large amount of gas has been processed into stars is supported by the presence of an "E +A" spectrum in the inner regions, evidence of a period of intense star formation less than 10^9 yr ago. This spectrum suggests a minimum burst strength of 10% and, in conjunction with considerations of the gas content, seems to allow burst strengths of up to 50% (Fritze-von Alvensleben & Gerhard 1993). Thus, several times 10^9 h^{-2} $\mathcal{M}_\odot$ of gas may have been processed into stars.

The presence of extended Hα emission in the remnant body and the detection of a central, possibly extended, x-ray source suggest that some of the H I may have been ionized and heated. Several studies indicate that gas is expected to reach x-ray temperatures because of heating by massive stars and supernovae following the merger-induced central burst of star formation (cf. Chevalier & Clegg 1985; Heckman *et al.* 1990), as well as in the interface of colliding molecular clouds (Harwit *et al.* 1987).

The strength of the x-ray emission seen in far-infrared bright galaxies (David *et al.* 1992) and in peculiar galaxies (Fabbiano *et al.* 1982) supports this idea. Moreover, hot gas produced by these mechanisms may shock heat any cold gas returning along the tidal tails (Spark 1992). Thus, the E+A spectrum, the central ionized- and molecular-gas disks, the extranuclear ionized gas, and the x-ray emission could all be related to the dearth of H I in the remnant body of NGC 7252.

4.4 From Spiral to Elliptical?

The large mass of H I found in the tidal tails and the smooth kinematics along the tails leave little doubt that NGC 7252 is the remnant of two merged, late-type spiral galaxies. Therefore, the hypothesis that two spiral galaxies can collide and merge into an elliptical-*like* remnant is strongly vindicated (see Sec. 1). It will probably be several dynamical times before the more obvious signs of tidal damage in NGC 7252 fade into the background to the point where the galaxy may lose its "peculiar" epithet. The "fine structure" (shells and ripples) that is seen in more than half of all field ellipticals (Schweizer 1992; Schweizer & Seitzer 1992) is expected to persist in NGC 7252 during this period. The question is: At the end of this time period, is it likely that NGC 7252 will be classified as a bona fide elliptical?

In order to address this question, we compare the present characteristics of NGC 7252 with several well-studied properties of elliptical galaxies.

(1) It is well established that NGC 7252 has an $r^{1/4}$ light profile in the optical V band (S82), in the near-infrared K band (Stanford & Bushouse 1991), and in B and R (see Fig. 6). Such a light distribution is characteristic of ellipticals (de Vaucouleurs 1953; Kormendy 1977) and is reproduced quite naturally in simulations of equal-mass mergers (Barnes 1988, 1992). Therefore, NGC 7252 serves to confirm that the stellar content of two merged spirals can be successfully redistributed into a relaxed distribution typical of elliptical galaxies.

(2) Lake & Dressler (1986) have shown that a sample of 16 merger remnants, including NGC 7252, obeys the Faber–Jackson relation (Faber & Jackson 1976) that is characteristic of normal elliptical galaxies. We find that NGC 7252 also lies in the more restrictive "fundamental plane" (Djorgovski & Davis 1987) defined by a series of relationships linking four observables of galaxies—mean surface brightness μ_e, effective radius r_e, absolute magnitude within this radius M_e, and stellar velocity dispersion σ_v—of which the Faber–Jackson relation (M_e vs σ_v) is a part. The quantities μ_e and r_e are obtained from the $r^{1/4}$ law that best approximates the light profile derived from ellipse fitting (see Sec. 3.2.1). This elliptical model also yields a value of $M_e = -21.3 + 5 \log h$ in the R band. Using these photometric parameters, along with $\sigma_v = 177$ km s^{-1} (Lake & Dressler 1986), NGC 7252 is found to fall well within the scatter of the relationships shown in Kormendy & Djorgovski (1989). Thus, NGC 7252 already appears to

be indistinguishable from a typical elliptical in the fundamental plane.

It is interesting in this context to see where NGC 7252 falls in the Tully–Fisher relation (Tully & Fisher 1977) that connects the luminosity of a spiral galaxy to its rotational linewidth. The maximum rotation velocity of the molecular disk of 110 km s^{-1} measured by WSS is corrected using an inclination of $41° \pm 9°$ derived by S82. We find that NGC 7252 lies outside the scatter of the relationship derived for spiral galaxies in the Ursa Major and Virgo clusters (Pierce & Tully 1988), even when one takes into account the considerable uncertainty in the inclination of its disk.

(3) Our study clearly illustrates that the H I from the spiral progenitors is restricted to the tidal tails and is absent from the main body. The present atomic gas content *in the remnant body* is $< 5 \times 10^7 \, h^{-2} \, \mathcal{M}_\odot$ and is typical of the upper limits for ellipticals (Knapp *et al.* 1985). The abrupt cutoff in the H I distribution at the apparent base of the NW tail suggests that there is ongoing conversion of the returning atomic gas into other forms—as long as this process continues, NGC 7252 will resemble an elliptical in its atomic gas content.

(4) The amount of $^{12}CO(1\rightarrow 0)$ currently observed in the central disk of NGC 7252 places it among the top 6% of ellipticals in its molecular-gas content (Lees *et al.* 1991). However, a moderate star-formation rate in the central molecular-gas disk, estimated to be about 1–2 $\mathcal{M}_\odot$ yr^{-1} on the basis of the infrared and radio continuum luminosity (Condon 1992), operating over the time it takes for the tidal features to fade could use up a lot of the available central reservoir of $3.5 \times 10^9 \, h^{-2} \, \alpha_{CO} \, \mathcal{M}_\odot$ of molecular gas.

(5) The *ROSAT* observations presented here measure for the first time the amount of x-ray emitting gas in NGC 7252. The x-ray luminosity in the 0.2–4.0 keV band is intermediate between that of a typical spiral and an elliptical of the same blue luminosity (Fabbiano *et al.* 1992), but the large scatter seen in the L_x vs L_B relations for normal galaxies makes the x-ray data inconclusive.

The conclusion then is that, as far as its photometric characteristics and the contents of different gas phases are concerned, NGC 7252 will probably resemble an elliptical galaxy in a few billion years.

4.5 Clumps in Tidal Tails

An old idea due to Zwicky (1956) suggests that bound subunits may be ejected during a tidal encounter and may survive in intergalactic space, perhaps taking on the form of dwarf irregulars, dwarf spheroidals, or full-sized irregular galaxies. This notion has received a fair amount of attention of late, particularly in numerical simulations (Gerola *et al.* 1983; Barnes & Hernquist 1992; Elmegreen *et al.* 1992). The recent theoretical efforts have been stimulated by the observation that clumps and giant H II regions, such as those found in the tails of NGC 7252, appear

to be ubiquitous in tidal features (Schweizer 1978; Hibbard & van Gorkom 1993; Mahoney *et al.* 1993; Mirabel *et al.* 1991, 1992).

The presence of much spatial structure in both the gas and stars in the tails of NGC 7252 and the obvious indications of localized star formation indicate that self-gravity must be playing a significant role in tidal clumps, perhaps even a dominant one. One might well ask: Do these regions have enough material to remain bound throughout the present star-forming episode? At present, about one-quarter ($\sim 5 \times 10^8 \, h^{-2} \, \mathcal{M}_\odot$) of the atomic gas in the tails is located in the vicinity of the giant H II regions. Whether or not these regions can retain this gas, or perhaps even enhance it by capturing more material in its vicinity, will have important consequences for the future evolution of these subsystems. In order for material to remain self-bound in the outer regions, a clump must have enough mass to: (1) hold itself together against its total internal kinetic energy; and (2) keep the material from being stolen back by the remnant.

The first condition requires that the total mass of the clump be larger than its virial mass $\mathcal{M}_{virial}$, where the virial mass is based on the internal energy of the material (using the one-dimensional velocity dispersion and assuming spherical symmetry) and the stretching shear of the tidal arm (estimated by dividing the velocities in the tails by their projected lengths). A correction has also been made to account for the velocity gradient across the beam.

The second condition requires that the tidal radius of the clump be greater than or equal to the radius containing the binding mass (Binney & Tremaine 1987). This condition may alternatively be expressed in terms of a tidal mass $\mathcal{M}_{tidal}$ needed to prevent material at the radial distance of the clumps from being tidally stripped by the remnant. For an estimate of $\mathcal{M}_{tidal}$, we adopt a remnant mass of 3×10^{11} $h^{-1} \, \mathcal{M}_\odot$ as suggested by the numerical modeling of this system (Mihos *et al.* 1993).

The resulting values of $\mathcal{M}_{virial}$ and $\mathcal{M}_{tidal}$ are given in Table 7 for both the NW and E clumps. Neither clump has enough material in gas alone to meet the virial criterion, with the NW/E clump requiring a factor of three/four times more mass, some of which might be provided by the stars and ionized gas seen in each clump. On the other hand, the measured mass of the gas alone is expected to be sufficient to keep the clumps from being tidally stripped by the remnant, despite the high remnant mass adopted (corresponding to a mass-to-light ratio of 10 $h \, \mathcal{M}_\odot / L_\odot$ for the remnant). Alternatively, if we assume that the clumps are marginally bound, the resulting mass-to-light ratios $\mathcal{M}_{virial}/L_B$ of the NW and E clumps are $3h$ and $7h \, \mathcal{M}_\odot / L_\odot$, respectively. These clumps represent impressive concentrations of atomic gas and young stars and the mass required to bind them, their H I mass, optical luminosity, linear size, and their velocity width are characteristic of dwarf irregular galaxies (cf. Hunter & Gallagher 1985; Freeman 1986).

The delicate interplay between gravity and the disruptive forces of star formation could make tidal tails lively arenas. This may explain why prominent optical conden-

sations are frequently found in such tails (S78), and why some tidal tails have gaps in their gas distribution (cf. Mahoney *et al.* 1993; Hibbard & van Gorkom 1994).

5. SUMMARY AND CONCLUSIONS

The following are the main points of this paper.

(1) VLA observations of the late-stage merger remnant NGC 7252 reveal $2 \times 10^9 \, h^{-2} \, \mathcal{M}_\odot$ of atomic hydrogen which is located exclusively in the outer, tidal regions of the galaxy: the two tails and the prominent western loop. No atomic gas is detected in the central relaxed stellar body.

(2) New *ROSAT* and Hα observations are also presented. In contrast to the H I distribution, the hot x-ray emitting plasma and molecular gas (mapped by WSS) are confined to the central region. Most of the Hα appears to be associated with the inner rotating molecular-gas disk ($r < 7''$), but some is seen to be associated with the base of the northwestern tail and with the western loop filling gap between the atomic and molecular gas distributions.

(3) The H I data yield the first detailed map of the kinematics of the tidal tails of NGC 7252 providing important new constraints on numerical simulations of this system. Each of the tidal features show remarkably smooth velocity gradients. We suggest that the material at the base of the northwestern tail is on a noncircular orbit, falling back towards the main remnant body. The H I observations may provide evidence for formation of shells and ripples by late-returning tidal material, and may explain some of the peculiar kinematics (e.g., line-of-slight velocity reversals) previously recorded in this system.

(4) The lack of neutral atomic hydrogen in the main body of the remnant, along with the presence of warm and hot ionized gas and a poststarburst spectrum in this region, suggests efficient, ongoing conversion of H I into other phases.

(5) Prominent Hα and H I, and stellar enhancements are seen in the tidal tails, each containing an amount of material similar to that seen in dwarf galaxies. If these clumps are bound, they serve to support the idea originally proposed by Zwicky (1956), and verified in recent numerical simulations, that dwarf galaxies can form from tidally ejected material.

(6) The long, gas-rich tidal tails of the NGC 7252 system imply two spiral progenitors. This evidence, combined with the photometric properties and gas content of NGC 7252, lends strong support to Toomre's (1977) suggestion that mergers of spirals can lead to elliptical-like remnants.

REFERENCES

Arp. H. C. 1966, ApJS, 14, 1
Baars, J. W. M., Genzel, R., Pauliny-Toth, I. I. K., & Witzel, A 1977, A&A, 61, 99
Barnes, J. E. 1988, ApJ, 331, 699
Barnes, J. E. 1992, ApJ, 393, 484
Barnes, J. E., & Hernquist, L. 1992, Nature, 360, 715
Binney, J., & Tremaine, S. 1987, Galactic Dynamics (Princeton University Press, Princeton)
Borne, K. D., & Richstone, D. O. 1991, ApJ, 369, 111
Braine, J., & Combes, F. 1993, A&A, 269, 7
Cayatte, V., Kotanyi, C., Balkowski, C., & van Gorkom, J. H. 1994, AJ (in press)
Chevalier, R. A., & Clegg, A. W. 1985, Nature, 317, 44
Condon, J. J. 1992, ARA&A, 30, 575
David, L. P., Jones, C., & Forman, W. 1992, ApJ, 388, 82
de Vaucouleurs, G. 1953, MNRAS, 113, 134
Djorgovski, S., & Davis, M. 1987, ApJ, 313, 59

Dressler, A., & Gunn, J. E. 1983, ApJ, 270, 7
Dupraz, C., Casoli, F., Combes, F., & Kazes, I. 1990, A&A, 228, L5
Elmegreen, B., Kaufmann, M., & Thomasson, M. 1993, ApJ (submitted)
Fabbiano, G., Feigelson, E., & Zamorani, G. 1982, ApJ, 256, 397
Fabbiano, G., Kim, D.-W., & Trinchieri, G. 1992, ApJS, 80, 531
Faber, S. M., & Jackson, R. E. 1976, ApJ, 204, 668
Freeman, K. C. 1986, in Nearly Normal Galaxies: From the Planck Time to the Present, edited by S. M. Faber (Springer, New York), p. 317
Fritze-von Alvensleben, U., & Gerhard, O. 1993, A&A (submitted)
Gerola, H., Carnevali, P., & Salpeter, E. E. 1983, ApJ, 268, L75
Gould, A., Guhathakurta, P., Richstone, D., & Flynn, C. 1992, ApJ, 388, 345
Guhathakurta, P., Tyson, J. A. 1989, ApJ, 346, 773
Harwit, M., Houck, J. R., Soifer, B. T., & Palumbo, G. G. C. 1987, ApJ, 315, 28
Heckman, T. M., Armus, L., & Miley, G. K. 1990, ApJS, 74, 833
Hernquist, L. 1992, ApJ, 400, 460

Hernquist, L., & Spergel, D. N. 1992, ApJ, 399, L117

Hibbard, J. E., & van Gorkom, J. H. 1993, in The Globular Cluster-Galaxy Connection, edited by G. H. Smith and J. P. Brodie (ASP Conference Series, Vol. 48), p. 619

Hibbard, J. E., & van Gorkom, J. H. 1994, in preparation

Hodge, P. 1993, in Massive Stars: Their Lives in the Interstellar Medium, edited by J. P. Cassinelli and E. B. Churchwell (ASP Conference Series, Vol. 35), p. 473

Hunter, D. A., & Gallagher, J. S., III 1985, ApJS, 58, 533

Kennicutt, R. C., Jr. 1984, ApJ, 287, 116

Kennicutt, R. C., Jr. 1992, ApJS, 79, 255

Knapp, G. R., Turner, E. L., & Cunniffe, P. E. 1985, AJ, 90, 454

Kormendy, J. 1977, ApJ, 218, 333

Kormendy, J., & Djorgovski, S. 1989, ARA&A, 27, 235

Kormendy, J., & Sanders, D. B. 1992, ApJ, 390, L53

Lake, G., & Dressler, A. 1986, ApJ, 310, 605

Lees, J. F., Knapp, G. R., Rupen, M. P., & Phillips, T. G. 1991, ApJ, 379, 117

Mahoney, J. H., van der Hulst, J. M., & Burke, B. F. 1993, in preparation

Maloney, P. 1989, in The Interstellar Medium in External Galaxies, edited by H. A. Thronson, Jr. and J. M. Shull (Kluwer, Dordrecht), p. 493

Mihos, J. C., Bothun, G. D., & Richstone, D. O. 1993, ApJ (in press)

Mirabel, I. F., Dottori, H., & Lutz, D. 1992, A&A, 256, L19

Mirabel, I. F., Lutz, D., & Maza, J. 1991, A&A, 243, 367

Pierce, M. J., & Tully, R. B. 1988, ApJ, 330, 579

Raymond, J., & Smith, B. 1977, ApJS, 35, 419

Sanders, D. B., Scoville, N. Z., Sargent, A. I., & Soifer, B. T. 1988, ApJ, 324, L55

Schombert, J. M., Wallin, J. F., & Struck-Marcell, C. 1990, AJ, 99, 497

Schweizer, F. 1978, in The Structure and Properties of Nearby Galaxies, IAU Symposium No. 77, edited by E. M. Berkhuijsen and R. Wielebinski (Reidel, Dordrecht), p. 279 (S78)

Schweizer, F. 1982, ApJ, 252, 455 (S82)

Schweizer, F. 1990, in Dynamics and Interactions of Galaxies, edited by R. Wielen (Springer, Heidelberg), p. 60

Schweizer, F. 1992, in Physics of Nearby Galaxies: Nature or Nurture?, edited by T. X. Thuan, C. Balkowski, and J. Trân Thanh Vân (Editions Frontieres, Gif-sur-Yvette)

Schweizer, F., & Ford, W. K., Jr. 1985, in New Aspects of Galaxy Photometry, edited by J.-L. Nieto (Lecture Notes in Physics No. 232), p. 145

Schweizer, F., & Seitzer, P. 1992, AJ, 104, 1039

Scoville, N. Z., Sanders, D. B., Sargent, A. I., Soifer, B. T., & Tinney, C. G. 1989, ApJ, 345, L25

Scoville, N. Z., Sargent, A. I., Sanders, D. B., & Soifer, B. T. 1991, ApJ, 366, L5

Solomon, P. M., & Sage, L. J. 1988, ApJ, 334, 613

Spark, W. 1992, ApJ, 399, 66

Stanford, S. A., & Bushouse, H. A. 1991, ApJ, 371, 92

Stark, A. A., Gammie, C. F., Wilson, R. W., Bally, J., Linke, R. A., Heiles, C., & Hurwitz, M. 1992, ApJS, 79, 77

Stetson, P. B. 1987, PASP, 99, 191

Toomre, A. 1977, in The Evolution of Galaxies and Stellar Populations, edited by B. M. Tinsley and R. B. Larson (Yale University Observatory, New Haven), p. 401

Toomre, A., & Toomre, J. 1972, ApJ, 178, 623 (TT)

Tully, R. B., & Fisher, R. 1977, A&A, 54, 661

Tyson, J. A., & Seitzer, P. 1988, ApJ, 335, 552

Wang, Z., Schweizer, F., & Scoville, N. Z. 1992, ApJ, 396, 510 (WSS)

Wevers, B. H. M. R., van der Kruit, P. C., & Allen, R. J. 1986, A&AS, 66, 505

Young, J. S. 1989, in The Interstellar Medium in External Galaxies, edited by H. A. Thronson, Jr., and J. M. Shull (Kluwer, Dordrecht), p. 67

Young, J. S., *et al.* 1986, ApJ, 311, L17

Zwicky, F. 1956, Ergebnisse der Exakten Naturwissenschaften, 29, 344